



A Two-moment Radiation Hydrodynamics Scheme Applicable to Simulations of Planet Formation in Circumstellar Disks

Julio David Melon Fuksman¹ , Hubert Klahr¹ , Mario Flock¹ , and Andrea Mignone² 

¹Max Planck Institute for Astronomy, Königstuhl 17, D-69117 Heidelberg, Germany; fuksman@mpia.de

²Dipartimento di Fisica, Università degli Studi di Torino, via Pietro Giuria 1, I-10125 Turin, Italy

Received 2020 May 4; revised 2020 November 3; accepted 2020 November 6; published 2021 January 11

Abstract

We present a numerical code for radiation hydrodynamics designed as a module for the freely available `PLUTO` code. We adopt a gray approximation and include radiative transfer following a two-moment approach by imposing the M1 closure to the radiation fields. This closure allows for a description of radiative transport in both the diffusion and free-streaming limits, and is able to describe highly anisotropic radiation transport as can be expected in the vicinity of an accreting planet in a protoplanetary disk. To reduce the computational cost caused by the timescale disparity between radiation and matter fields, we integrate their evolution equations separately in an operator-split way, using substepping to evolve the radiation equations. We further increase the code's efficiency by adopting the reduced speed of light approximation (RSLA). Our integration scheme for the evolution equations of radiation fields relies on implicit-explicit schemes, in which radiation-matter interaction terms are integrated implicitly while fluxes are integrated via Godunov-type solvers. The module is suitable for general astrophysical computations in one, two, and three dimensions in Cartesian, spherical, and cylindrical coordinates, and can be implemented on rotating frames. We demonstrate the algorithm performance on different numerical benchmarks, paying particular attention to the applicability of the RSLA for computations of physical processes in protoplanetary disks. We show 2D simulations of vertical convection in disks and 3D simulations of gas accretion by planetary cores, which are the first of their kind to be solved with a two-moment approach.

Unified Astronomy Thesaurus concepts: [Radiative transfer \(1335\)](#); [Protoplanetary disks \(1300\)](#); [Planet formation \(1241\)](#)

1. Introduction

Radiative transfer is a key tool to understand the dynamics and observational properties of almost any astrophysical system. In protostellar disks, the study of radiative processes is a necessary ingredient to predict which zones are able to develop different hydrodynamical instabilities that lead to turbulence and consequent transport of angular momentum, structure formation, and eventual growth of planets (see, e.g., Gammie 1996; Flock et al. 2017; Manger & Klahr 2018; Pfeil & Klahr 2019). Some processes, such as diffusive cooling or the radiative processes occurring in the vicinity of gap-opening planets, may involve transport of radiation between optically thick and optically thin regions. This can in principle lead to anisotropic transport regimes involving highly beamed radiative intensities, which require a proper treatment that allows for such directional transport. On the other hand, a self-consistent treatment of stellar irradiation and dust absorption, emission, and scattering of radiation coupled to gas dynamics is needed to explain the current observations of disk substructures at increasingly high resolution in the thermal dust emission (see, e.g., ALMA Partnership et al. 2015; Flock et al. 2015).

The coupled integration of hydrodynamics (HD) and frequency-dependent radiative transfer is in general a computationally expensive task, and approximate methods are most usually preferred. A generally adopted assumption is the gray approximation, in which the radiative intensity and the material absorption and scattering opacity coefficients are averaged in the frequency domain. This approach leads to a description of total energy and momentum exchange between matter and radiation, without regarding frequency-dependent phenomena. The applicability of the gray approximation is tied to the

variation of the material's opacity with frequency in the spectral region of interest, and is therefore case-dependent.

Among all gray radiative transfer schemes, the flux-limited diffusion (FLD) method by Levermore & Pomraning (1981) is the most widely preferred method in the context of protoplanetary disks and star formation in general. This is a one-moment method, meaning that the full radiative transfer equation is turned into a single evolution equation for one of the moments (angular integrals) of the specific radiative intensity, in this case, the radiation energy density. In FLD, the radiation flux is computed via an ad hoc function of the radiation energy density, its gradient, and the material's local opacity, in such a way that the module of the flux tends to its correct limit in the diffusion and free-streaming regimes. This method is particularly accurate in highly opaque systems, where the radiation transport equation correctly tends to a diffusion equation. Conversely, due to the adopted definition of the radiation flux, some degree of inaccuracy is generally observed in regions of low opacity (Rosdahl & Teyssier 2015). On the other hand, FLD methods are unable to describe strongly anisotropic transport in phenomena such as shadows or simply free-streaming, in which cases they introduce unphysical numerical diffusion due to the fact that the radiation flux is always proportional to the gradient of the energy density (Hayes & Norman 2003).

To make predictions on the observational appearance of accreting planets (Szulágyi et al. 2018, 2019) and to reconstruct the characteristics of exoplanets from observations of disks around young stars, one needs a combination of radiation hydrodynamical simulations in the gray approximation, as we can provide in this paper, and detailed Monte Carlo continuum radiative transfer simulations, as presented by our collaboration

partners Krieger & Wolf (2020). In subsequent works, we intend to connect in this way realistic flow and temperature structures with frequency-dependent intensity maps for various instruments such as the Atacama Large Millimeter/submillimeter Array (ALMA; Kurz et al. 2002), and the Very Large Telescope Interferometer (VLTI) instruments PIONIER (Le Bouquin et al. 2011) and MATISSE (Lopez et al. 2014). On the other hand, the growth timescale of gas planets (Mordasini et al. 2012) depends on the efficiency of radiative cooling (D’Angelo & Bodenheimer 2013; Szulágyi et al. 2014, 2016; Szulágyi & Mordasini 2017; Schulik et al. 2020) and therefore a better understanding of possible gas accretion rates also in the presence of pebble (Klahr & Bodenheimer 2006; Ormel & Klahr 2010; Lambrechts & Johansen 2012) and planetesimal accretion (Fortier et al. 2013) will have a strong impact on the ability to form efficiently gas giants. Due to the mentioned low opacity regimes occurring, e.g., in planetary gaps, it is ideal to count with radiation transport schemes that do not rely on a pure diffusion approximation.

In this work we have implemented the two-moment approach by Levermore (1984), generally referred to as M1 closure. In this method, an additional set of equations is solved for the radiation flux components, where this time the radiation pressure tensor is defined in terms of the radiation flux and energy density. This closure is based on the assumption that the specific radiative intensity is isotropic in a given reference frame, and hence it yields exact flux values if such assumption is correct. Despite this is often a fairly reasonable approximation, it must be noted that this assumption fails to describe cases where such a reference frame does not exist. This happens, for instance, when optically thin regions of space have converging beams that originate from different directions, in which case the M1 closure produces unphysical interactions between the beams (see, e.g., Sądowski et al. 2013; Skinner & Ostriker 2013). Another important advantage of this closure is that freely streaming radiation fields are transported maintaining their original direction, without being artificially spread as in FLD methods. On the other hand, both methods yield the same diffusion equation in largely opaque media. From the numerical point of view, the M1 closure counts with the advantage that the evolution equations are hyperbolic with local interaction source terms, whereas the FLD equations are parabolic and usually solved via fully implicit methods (see Commerçon et al. 2011). Hence, unless fully implicit schemes are used to solve the evolution equations, M1 methods should have favorable scaling properties when compared to FLD.

We have implemented a two-moment radiation HD (Rad-HD) module within the multi-algorithm, high-resolution code PLUTO, designed for time-dependent computations of relativistic or nonrelativistic unmagnetized or magnetized flows (Mignone et al. 2007). The module is fully parallel, and can be applied using Cartesian, cylindrical, and spherical coordinate systems in one, two, or three-dimensions. Our current implementation is an extension of the module for radiation relativistic magnetohydrodynamics (Rad-RMHD) introduced in Melon Fuksman & Mignone (2019), where implicit-explicit (IMEX) schemes have been used to integrate the evolution equations in such a way that fluxes are integrated explicitly, while the potentially stiff radiation-matter interaction terms are integrated implicitly. In that case, the time step is computed as a minimum of the maximum time steps allowed for the transport of radiation and magnetohydrodynamical fields,

obtained in each case by applying the Courant–Friedrichs–Lewy (CFL) stability condition (Courant et al. 1928). Contrarily, in our case, radiation and nonrelativistic flows evolve in largely different timescales, which renders that approach computationally prohibitive and largely diffusive due to the accumulation of truncation error. To reduce the computational cost, we follow a twofold strategy. On the one hand, we adopt the reduced speed of light approximation (RSLA), introduced by Gnedin & Abel (2001) and applied to M1 Rad-HD by Skinner & Ostriker (2013), in which the value of the speed of light is replaced by an artificially low value in order to reduce the mentioned scale disparity. This increases the maximum time step allowed by the CFL condition, consequently reducing the overall cost of the operations. The RSLA is valid as long as the chosen reduced value of the speed of light is larger than any velocity scale in the problem at hand, in which case it yields the same solutions that would be obtained using its physical value. Since this restriction maintains some disparity between the mentioned timescales, we further reduce the computational cost of the method by applying operator splitting to solve the HD and radiation equations in different steps. We use in each case the corresponding time step restriction given by the CFL condition and apply substepping to solve the radiation subsystem, using IMEX schemes to integrate the radiation fields.

Additional features of the code include an adaptation of the Harten–Lax–van Leer-contact (HLLC) solver for radiation transport introduced in Melon Fuksman & Mignone (2019) and an implementation of the second-order accurate IMEX-SSP2 (2,2,2) scheme by Pareschi & Russo (2005), also implemented in the general relativistic code by McKinney et al. (2014), both of which represent improvements with respect to other existing M1 methods, such as that introduced by Skinner & Ostriker (2013). Furthermore, the numerical diffusion introduced by the operator-split radiative transfer scheme applied in that work causes shadow profiles to be appreciably less defined than those obtained with the IMEX schemes implemented in our module (see Melon Fuksman & Mignone 2019). On the other hand, the code can be applied to solve the Rad-HD equations in a rotating frame following the conservative formulation described in Mignone et al. (2012a), under the condition that the relativistic corrections appearing when transforming the radiative transport equations into such frame can be disregarded. This feature is particularly useful in planet formation scenarios to limit the numerical diffusion in the vicinity of accreting planets. Even though it is our particular interest to apply our module to such systems, its applicability is rather general, and it will be included in future versions of PLUTO.

Several two-moment Rad-HD implementations can be found in the literature (see, e.g., Audit et al. 2002; Hayes & Norman 2003; González et al. 2007; Jiang et al. 2012; Sądowski et al. 2013; Skinner & Ostriker 2013; Takahashi & Ohsuga 2013; McKinney et al. 2014; Rosdahl & Teyssier 2015; Melon Fuksman & Mignone 2019; Mignon-Risse et al. 2020; Weih et al. 2020). To our knowledge, these methods have not been applied to model protoplanetary disk evolution and planet formation scenarios other than in Voelkel (2017). Note that these authors implemented a fully implicit scheme, which does not make use of the reduced speed of light ansatz, yet makes global parallelization and adaptive mesh refinement less efficient. An interesting application in the context of star formation is shown in Mignon-Risse et al. (2020), where the

formation of a disk following the collapse of a massive prestellar core is studied using a hybrid method in which stellar irradiation is modeled with an M1 scheme, while gas reemission and absorption is treated via FLD. In this work, we have studied different applications of our module to global simulations of protoplanetary disks, paying special attention to the applicability of the RSLA in this context. In particular, we have modeled the growth of the vertical convective instability in a disk and the accretion of gas onto a planetary core.

This paper is organized as follows. In Section 2, we summarize the main equations characterizing our model and discuss the main features and limitations of the RSLA, while in Section 3 we describe the implemented algorithms. In Section 4, we test the code's performance on different numerical benchmarks and study different applications in the context of protoplanetary disks. In Section 5, we summarize the main results of our work. Additional performance tests and comparisons to other methods are included in the Appendix.

2. Governing Equations

2.1. Rad-HD

Throughout this work we solve the equations of a fluid interacting with a radiation field, for which we follow a two-moment approach under the gray approximation. The resulting evolution equations, namely the Rad-HD equations, can be written in quasi-conservative form as

$$\begin{aligned} \frac{\partial \rho}{\partial t} + \nabla \cdot (\rho \mathbf{v}) &= 0 \\ \frac{\partial(\rho \mathbf{v})}{\partial t} + \nabla \cdot (\rho \mathbf{v} \mathbf{v}) + \nabla p_g &= \mathbf{G} + \mathbf{S}_m - \rho \nabla \Phi \\ \frac{\partial(E + \rho \Phi)}{\partial t} + \nabla \cdot [(E + p_g + \rho \Phi) \mathbf{v}] &= c G^0 + S_E - \nabla \cdot \mathbf{F}_{\text{irr}} \\ \frac{1}{\hat{c}} \frac{\partial E_r}{\partial t} + \nabla \cdot \mathbf{F}_r &= -G^0 \\ \frac{1}{\hat{c}} \frac{\partial \mathbf{F}_r}{\partial t} + \nabla \cdot \mathbb{P}_r &= -\mathbf{G}, \end{aligned} \quad (1)$$

where ρ , p_g , and \mathbf{v} are the fluid's density, pressure, and velocity, while E_r , \mathbf{F}_r , and \mathbb{P}_r are respectively the radiation energy, flux, and pressure tensor. The gas energy density E is defined in terms of these fields as

$$E = \rho \epsilon + \frac{1}{2} \rho \mathbf{v}^2, \quad (2)$$

where $\rho \epsilon$ is the gas internal energy density. On the other hand, radiation fields are defined in terms of the frequency- and direction-dependent radiation specific intensity $I_\nu(t, \mathbf{x}, \mathbf{n})$, as

$$\begin{aligned} E_r &= \frac{1}{c} \int_0^\infty d\nu \oint d\Omega I_\nu(t, \mathbf{x}, \mathbf{n}) \\ F_r^i &= \frac{1}{c} \int_0^\infty d\nu \oint d\Omega I_\nu(t, \mathbf{x}, \mathbf{n}) n^i \\ P_r^{ij} &= \frac{1}{c} \int_0^\infty d\nu \oint d\Omega I_\nu(t, \mathbf{x}, \mathbf{n}) n^i n^j \end{aligned} \quad (3)$$

(see Mihalas & Mihalas 1984), in such a way that all three quantities are measured in units of energy density. Additionally, we have included a gravitational potential Φ , which is

defined as a general function of the spatial coordinates. The constants c and \hat{c} correspond, respectively, to the speed of light and its reduced value (see Section 2.3). In our implementation, these equations can be solved in Cartesian, cylindrical, or spherical coordinates.

Several source terms are included on the right-hand side of Equation (1), beginning with the radiation-matter interaction terms G^0 and \mathbf{G} . In the gray approximation, these can be written in the fluid's comoving frame as

$$\begin{aligned} \tilde{G}^0 &= \kappa \rho (\tilde{E}_r - a_R T^4) \\ \tilde{\mathbf{G}} &= \chi \rho \tilde{\mathbf{F}}_r, \end{aligned} \quad (4)$$

where $a_R = \sigma_{\text{SB}}/\pi c$ is the radiation constant, σ_{SB} the Stefan–Boltzmann constant, T the gas temperature, and κ , σ , and $\chi = \kappa + \sigma$ are, respectively, the frequency-averaged absorption, scattering, and total opacity coefficients, which can be defined as general functions of ρ and T . It is customary to compute κ and χ in Equation (4), respectively, as their Planck and Rosseland means, since the first of these choices is particularly accurate for low opacities while the second one yields the correct flux in the diffusion regime (Mihalas & Mihalas 1984). For testing purposes, unless otherwise stated, we take these averages to be equal, and use single values for κ , σ , and χ keeping in mind that the actual values can be largely different when different averaging procedures are applied (see, e.g., Malygin et al. 2014). Opacity coefficients, together with quantities under tilde, are measured in the comoving frame, whereas every other quantity is measured in the laboratory frame. Gas temperatures are computed following the ideal law

$$T = \frac{\mu u p_g}{k_B \rho}, \quad (5)$$

where μ is the gas mean molecular weight, u is the atomic mass unit, and k_B is the Boltzmann constant. We compute the interaction terms in the laboratory frame by making use of the following Lorentz transformation laws to first order in $\beta = \mathbf{v}/c$:

$$\begin{aligned} G^0 &= \tilde{G}^0 + \beta \cdot \tilde{\mathbf{G}} \\ \mathbf{G} &= \tilde{\mathbf{G}} + \tilde{G}^0 \beta. \end{aligned} \quad (6)$$

Similarly, the radiation fields are transformed into the laboratory frame to first order in β , as

$$\begin{aligned} E_r &= \tilde{E}_r + 2\beta_i \tilde{F}_i \\ F_r^i &= \tilde{F}_r^i + \beta^i \tilde{E}_r + \beta_j \tilde{P}_r^{ij} \\ P_r^{ij} &= \tilde{P}_r^{ij} + \beta^i \tilde{F}_r^j + \beta^j \tilde{F}_r^i. \end{aligned} \quad (7)$$

This yields the following expressions for the interaction terms that are used in the code:

$$\begin{aligned} G^0 &= \rho \kappa (E_r - a_R T^4 - 2\beta \cdot \mathbf{F}_r) \\ &\quad + \rho \chi \beta \cdot (\mathbf{F}_r - E_r \beta - \beta \cdot \mathbb{P}_r) \\ \mathbf{G} &= \rho \kappa (E_r - a_R T^4 - 2\beta \cdot \mathbf{F}_r) \beta \\ &\quad + \rho \chi (\mathbf{F}_r - E_r \beta - \beta \cdot \mathbb{P}_r), \end{aligned} \quad (8)$$

where we have kept some $\mathcal{O}(\beta^2)$ terms in order to recover the local thermal equilibrium (LTE) limit given by $\tilde{E}_r \rightarrow a_R T^4$ and

$\tilde{F}_r \rightarrow \mathbf{0}$ when $\sigma, \kappa \rightarrow \infty$ (similar approaches are followed in Lowrie et al. 1999; Jiang et al. 2012).

An irradiation term $-\nabla \cdot \mathbf{F}_{\text{Irr}}$ is included in Equation (1) to account for radiative heating caused by sources emitting in a different frequency range than the one considered in the radiation transport scheme. One such example is the heating from star irradiation in protoplanetary disks, in which the radiation coming from the star peaks in the visible range, but most of the energy emitted by the dust is in the infrared. This additional flux is not updated by solving an evolution equation, but it is instead computed at each time step as a function of space.

Finally, the terms S_E and S_m account for dissipative effects included in the current version of PLUTO, such as thermal conduction, optically thin cooling, and viscosity (Mignone et al. 2012b). In the latter case, these terms take the form

$$\begin{aligned} S_m &= \nabla \cdot \Pi \\ S_E &= \nabla \cdot (\mathbf{v} \cdot \Pi), \end{aligned} \quad (9)$$

where Π is the viscosity tensor defined as

$$\Pi = \rho \nu_1 [\nabla \mathbf{v} + (\nabla \mathbf{v})^\top] + \rho \left(\nu_2 - \frac{2}{3} \nu_1 \right) (\nabla \cdot \mathbf{v}) \mathbb{I}, \quad (10)$$

where \mathbb{I} is the identity matrix, while ν_1 and ν_2 are, respectively, the shear and bulk viscosity coefficients.

In cylindrical and spherical coordinates, Equation (1) can be integrated in a reference frame that rotates with a uniform angular velocity Ω . The integration of the additional terms that appear when applying Galilean transformations to the HD fields follows the conservative formulation detailed in Mignone et al. (2012a). On the other hand, E_r and \mathbf{F}_r follow the transformation law given by Equation (7), and therefore all additional terms arising from this transformation are of order $\Omega R/c$, where R is the cylindrical radius. In the current form of the module we do not include such additional terms, which means that the rotating frame scheme can only be applied when terms of order β can be disregarded, as is typically the case in planet formation scenarios (see, e.g., Section 4.4). This means that, in such cases, the radiation-matter interaction terms are equal to their comoving values (Equation (4)). However, since the relativistic corrections to the HD equations are of order β^2 , we keep in general all terms of order β in Equation (8) to account for mildly relativistic cases where β^2 can be disregarded.

2.2. Closure Relations

The Rad-HD system of equations (Equation (1)) is completely defined by imposing a series of closure relations. For HD quantities, we impose the equation of state of an ideal gas,

$$\rho \epsilon = \frac{P_g}{\Gamma - 1}, \quad (11)$$

with a constant specific heat ratio Γ . For the radiation fields, we implement the M1 closure (Levermore 1984), in which the components of the pressure tensor can be computed in terms of E_r and \mathbf{F}_r as

$$P_r^{ij} = D^{ij} E_r, \quad (12)$$

where the Eddington tensor is defined as

$$D^{ij} = \frac{1 - \xi}{2} \delta^{ij} + \frac{3\xi - 1}{2} n^i n^j, \quad (13)$$

with

$$\xi = \frac{3 + 4f^2}{5 + 2\sqrt{4 - 3f^2}}, \quad (14)$$

where $\mathbf{n} = \mathbf{F}_r / \|\mathbf{F}_r\|$, $f = \|\mathbf{F}_r\|/E_r$, and δ^{ij} is the Kronecker delta. With these definitions, the radiation fields correctly reproduce both the free-streaming limit when $\|\mathbf{F}_r\| \rightarrow E_r$, in which case $P_r^{ij} = E_r n^i n^j$, and the diffusion limit when $\|\mathbf{F}_r\| \ll E_r$, which gives the Eddington approximation $P_r^{ij} = (\delta^{ij}/3)E_r$. The latter case is verified for large opacities, in which case the last two of Equation (1) yield the diffusion equation

$$\frac{\partial E_r}{\partial t} \approx \nabla \cdot \left(\frac{\hat{c}}{3\rho\chi} \nabla E_r \right) \quad (15)$$

for slow variations of $\partial_t \mathbf{F}_r$. Equation (15) shows that the diffusion coefficient has been artificially reduced by a factor c/\hat{c} , which limits the applicability of this method to cases that are at most weakly dependent on its physical value, as detailed in Section 2.3.

2.3. The RSLA

The RSLA consists in choosing a value of \hat{c} smaller than c , in such a way to reduce the computational cost of integrating Equation (1) (see Section 3). This formalism has the drawback of introducing unphysical phenomena, the most evident one being that the propagation velocity of freely streaming radiation fields is \hat{c} instead of c . On the other hand, radiation-matter interaction timescales such as thermal equilibrium and diffusion timescales are increased (see, e.g., Equation (15)). Another important consequence of this approach is that the usual form of the conservation of total energy-momentum is lost. Disregarding gravity and all nonideal source terms in Equation (1) except for the radiation-matter interaction terms, we can obtain conservation laws for the fields

$$\begin{aligned} E_{\text{tot}} &= E + (c/\hat{c})E_r \\ \mathbf{m}_{\text{tot}} &= \rho \mathbf{v} + (1/\hat{c})\mathbf{F}_r, \end{aligned} \quad (16)$$

which are only equal to the total energy and momentum densities if $\hat{c} = c$. Still, the RSLA yields exact stationary solutions of Equation (1), since \hat{c} does not appear in them if all time derivatives are set to zero. More generally, the RSLA yields exact solutions of the Rad-HD equations provided radiation-matter interaction occurs much faster than any timescale of interest in the problem at hand.

A rather general criterion for the applicability of the RSLA has been derived in Skinner & Ostriker (2013), by requiring that the existing timescale hierarchies remain unchanged when c is replaced by \hat{c} . This condition is satisfied under the conditions that the value of \hat{c} remains much larger than the maximum fluid velocity v_{max} and that the diffusion timescale $t_{\text{diff}} = L\tau_{\text{max}}/\hat{c}$ is much smaller than the dynamical timescale $t_{\text{dyn}} = L/v_{\text{max}}$, where L and τ_{max} are a typical length and optical depth of the system.

These constraints can be summarized as

$$\hat{c} \gg v_{\max} \max(1, \tau_{\max}). \quad (17)$$

However, it must be noted that this is an approximate relation, and that the determination of an optimal \hat{c} value depends in general on the problem at hand, and can only be safely achieved through careful testing (see, e.g., Section 4.1).

Using Equation (17), we can evaluate the applicability of the RSLA to simulations of protoplanetary disks. To this purpose, we consider a disk with a superficial density $\Sigma_{1\text{ au}}^{\text{dust}} \sim 10 \text{ g cm}^{-2}$ undergoing changes that propagate at $v_{\max} \sim c_s/10$, where $c_s \sim 1 \text{ km s}^{-1}$. Assuming a vertical Gaussian profile at a radius $R = 1 \text{ au}$ with $H/R = 0.05$, where H is the pressure scale height, we have computed the optical depth in the vertical direction in an inner zone given by $z \in [-H, H]$ and an outer zone given by $z \in [H, 4H]$, using a mean absorption opacity $\kappa \sim 400 \text{ cm}^2 \text{ g}^{-1}$. This gives the conditions $\hat{c} \gg c/1100$ for the inner zone and $\hat{c} \gg c/4700$ for the outer zone. The effect of the choice of \hat{c} in this context is further studied in Section 4.

3. Numerical Scheme

3.1. Outline of the Algorithm

Our integration scheme consists of two main steps: the HD step, given by the integration of the subsystem

$$\frac{\partial \mathcal{U}_{\text{HD}}}{\partial t} + \nabla \cdot \Phi_{\text{HD}} = \mathcal{S}_{\text{HD}}, \quad (18)$$

and a radiation step, consisting of the integration of the radiation transport and interaction terms as

$$\begin{aligned} \frac{1}{\hat{c}} \frac{\partial \mathcal{U}_r}{\partial t} + \nabla \cdot \Phi_r &= -\mathcal{G} \\ \frac{\partial}{\partial t} \left(\frac{E}{\rho v} \right) &= \mathcal{G}, \end{aligned} \quad (19)$$

where $\mathcal{U}_{\text{HD}} = (\rho, \rho v, E + \rho \Phi)^\top$ and $\mathcal{U}_r = (E_r, \mathbf{F}_r)^\top$ are, respectively, the HD and radiation conserved fields, $\Phi_{\text{HD}} = (\rho v, \rho v v + p_g \mathbb{I}, (E + p_g + \rho \Phi) \mathbf{v})^\top$ and $\Phi_r = (\mathbf{F}_r, \mathbb{P}_r)^\top$ are the HD and radiation fluxes, and the source terms are defined as $\mathcal{S}_{\text{HD}} = (0, \mathbf{S}_m, S_E - \nabla \cdot \mathbf{F}_{\text{irr}})^\top$ and $\mathcal{G} = (G^0, \mathbf{G}^\top)^\top$.

Following the second-order operator splitting scheme by Strang (1968), our algorithm is divided in three consecutive integration steps, beginning by a radiation step with a time increment $\Delta t = \Delta t_{\text{HD}}^n/2$, followed by an HD step with $\Delta t = \Delta t_{\text{HD}}^n$ and a final radiation step with $\Delta t = \Delta t_{\text{HD}}^n/2$. For each time step n , the time increment Δt_{HD}^n is updated applying the CFL condition to the subsystem given by Equation (18), implemented as

$$\Delta t_{\text{HD}}^{n+1} = C_a \min_{ijk} \left[\frac{1}{N_{\text{dim}}} \sum_d \frac{\lambda_{\text{HD}}^d}{\Delta l^d} \right]^{-1}, \quad (20)$$

where Δl^d and λ_{HD}^d are the cell width and maximum signal speed of the HD subsystem along the direction d at the position (i, j, k) , while C_a is the Courant factor and N_{dim} is the number of dimensions. Each radiation step is divided into N_r integration

substeps, where the time increments are updated as

$$\begin{aligned} \Delta t_r^{n,q+1} \\ = \min \left[C_a \min_{ijk} \left[\frac{1}{N_{\text{dim}}} \sum_d \frac{\lambda_r^d}{\Delta l^d} \right]^{-1}, \frac{\Delta t_{\text{HD}}^n}{2} - \sum_{s=1}^q \Delta t_r^{n,s} \right], \end{aligned} \quad (21)$$

in such a way that they verify the CFL condition and also satisfy

$$\sum_{q=1}^{N_r} \Delta t_r^{n,q} = \frac{\Delta t_{\text{HD}}^n}{2}, \quad (22)$$

where now λ_r^d is the maximum signal speed of the radiation subsystem (Equation (19)), typically of the same order of magnitude as \hat{c} . This method, similar to that applied in Skinner & Ostriker (2013), reduces the computational overhead of the HD step if compared to an IMEX scheme applied to the full system of Rad-HD equations, since the radiation and HD time steps generally satisfy $\Delta t_r^{n,q} \ll \Delta t_{\text{HD}}^n$ (see Equations (17), (20), and (21)). We describe the integration methods implemented in the HD and radiation steps in Sections 3.2 and 3.3.

3.2. HD Step

Except for the irradiation term, Equation (18) contains the system of equations solved by the HD module of PLUTO, and hence its integration scheme remains unchanged with respect to that implemented in the code (see Mignone et al. 2007). We follow a finite volume approach, in which the cell-averaged values of the conserved fields are explicitly integrated by means of total variation diminishing (TVD) Runge–Kutta schemes (Gottlieb & Shu (1996)), making use of Godunov-type solvers to compute fluxes at zone interfaces. To this purpose, volume averages are reconstructed at cell boundaries using piecewise monotonic interpolants inside each computational cell.

During the HD step, all source terms are computed at cell centers and explicitly integrated together with flux divergences. If irradiation is implemented, the value of \mathbf{F}_{irr} is updated at each time step according to the current mass distribution, and its divergence is stored at cell centers for its integration. On the other hand, parabolic source terms such as the viscosity terms in Equation (9) can be either explicitly integrated in a single time step or in several substeps by means of one of the super-time-stepping (STS) techniques introduced in Alexiades et al. (1996) and Meyer et al. (2012), whose implementation in PLUTO is discussed in Mignone et al. (2007) and Vaidya et al. (2017). If STS is used, the HD time increment is computed following Equation (20), otherwise being reduced following the prescription by Beckers (1992) to account for additional stability conditions for the integration of parabolic terms.

3.3. Radiation Step

The methods followed during the radiation step are based on those implemented in Melon Fuksman & Mignone (2019). In this work, Equation (19) is integrated by means of IMEX-Runge–Kutta schemes, which consist of modified Runge–Kutta schemes in which all fluxes are integrated explicitly, while radiation-matter interaction terms are integrated implicitly. In particular, we have implemented the IMEX-SSP2(2,2,2) method by Pareschi & Russo (2005), and the IMEX1 method

employed in Melon Fuksman & Mignone (2019), also implemented by Bucciantini & Del Zanna (2013) in the context of resistive general relativistic magnetohydrodynamics. These methods are of order 2 and 1 in time and L- and A-stable, respectively, which makes IMEX-SSP2(2,2,2) a more robust option in some applications, being stable for larger values of C_a . On the other hand, IMEX1 seems to be a more accurate option able to balance out advection and interaction terms in problems where both are much larger than their difference, as is the case in diffusion problems (Melon Fuksman & Mignone 2019). Both methods are further compared in Appendix A.1, where they are used to compute the evolution of damped linear radiation waves.

During each explicit step of the mentioned IMEX schemes, an equation of the form

$$\frac{1}{\hat{c}} \frac{\partial \mathcal{U}_r}{\partial t} + \nabla \cdot \Phi_r = 0 \quad (23)$$

is explicitly integrated by applying a TVD Runge–Kutta scheme and using Godunov-type solvers to compute fluxes at zone interfaces, as done in the HD step. We implemented three different Riemann solvers: a Lax–Friedrichs–Rusanov solver (see, e.g., Toro 2009), the Harten–Lax–van Leer (HLL) solver by González et al. (2007), and the HLLC solver introduced in Melon Fuksman & Mignone (2019). Characteristic radiation velocities are computed as described in Audit et al. (2002) and Skinner & Ostriker (2013), and limited in optically thick cells in order to minimize numerical diffusion according to the prescription introduced in Sądowski et al. (2013). The upper limit to the radiation flux given by the physical constraint

$$||\mathbf{F}_r|| \leq E_r \quad (24)$$

is imposed on cell boundaries during the reconstruction step. On the other hand, geometrical source terms that arise from the expression of the divergence in curvilinear coordinates are explicitly integrated during the explicit step.

All remaining terms in Equation (19) are integrated in the implicit step. To do so, we rearrange this equation in the following way:

$$\frac{\partial \mathcal{U}_r}{\partial t} = -\hat{c} \mathcal{G}, \quad \frac{\partial}{\partial t} \begin{pmatrix} E_{\text{tot}} \\ \mathbf{m}_{\text{tot}} \end{pmatrix} = 0, \quad (25)$$

where E_{tot} and \mathbf{m}_{tot} are defined in Equation (16). We implicitly integrate the first of these equations while keeping E_{tot} and \mathbf{m}_{tot} constant. Each implicit step in the IMEX schemes can be written as

$$\mathcal{U}_r = \mathcal{U}'_r - s \Delta t_r^{n,a} \hat{c} \mathcal{G}, \quad (26)$$

where s is a constant and \mathcal{U}'_r denotes an intermediate-state value. Since during this step E_{tot} and \mathbf{m}_{tot} must remain constant, HD fields can be defined as functions of the radiation fields and vice versa by inverting Equation (16). Therefore, Equation (26) can be solved through iterative methods that update either \mathcal{U}_r or some set of HD fields that allows the inversion of Equation (16) to obtain \mathcal{U}_r .

We implemented three implicit methods, namely, Newton–Rad, Newton–HD, and fixed point (FP). The first two of these correspond to Newton methods iterating, respectively, \mathcal{U}_r and $(p_g, \mathbf{v})^T$, while the last one is a fixed-point method based on iterations of \mathcal{U}_r . Both Newton–Rad and Newton–HD present no

major changes with respect to their implementation in Melon Fuksman & Mignone (2019), except for the different form of the Jacobian due to our expansion of the source terms up to order β^2 (Equation (8)). Similar implementations can be found in McKinney et al. (2014) and Sądowski et al. (2013). The FP method was introduced in Palenzuela et al. (2009) in the context of resistive relativistic magnetohydrodynamics and implemented in Melon Fuksman & Mignone (2019) for Rad–RMHD, having been first applied in this context in Takahashi & Ohsuga (2013). This scheme is based on a linearization of Equation (26) achieved by writing all HD variables and the Eddington tensor D^{ij} at a previous iteration with respect to \mathcal{U}_r . In that manner, \mathcal{G} can be written at a given iteration m as

$$\mathcal{G}^{(m)} = \mathcal{M}^{(m)} \mathcal{U}_r^{(m+1)} + b^{(m)}, \quad (27)$$

where

$$\mathcal{M} = \begin{pmatrix} \rho\kappa - \rho\chi(\beta^2 + \beta_k\beta_l D_{kl}) & \rho(\sigma - \kappa)\beta_j \\ -\rho\sigma\beta_i - \rho\chi\beta_k D_{ik} & \rho\chi\delta_{ij} - 2\rho\kappa\beta_i\beta_j \end{pmatrix}, \quad (28)$$

and $b = -\kappa \rho a_R T^4(1, \beta)^T$. Finally, \mathcal{U}_r can be updated as

$$\mathcal{U}_r^{(m+1)} = (\mathcal{I} + s \Delta t_r^n \mathcal{M}^{(m)})^{-1} (\mathcal{U}'_r - s \Delta t_r^n b^{(m)}), \quad (29)$$

after which HD fields can be updated by inverting Equation (16) and the process can be repeated until convergence is reached. A convergence criterion is imposed in each method by requiring that the relative variation of the iterated fields becomes lower than a given threshold. To avoid accuracy issues that may arise when E_r and E are different by several orders of magnitude (see, e.g., McKinney et al. 2014), we have added the option of imposing the same criterion to the relative variations of p_g in Newton–Rad and FP, doing the same with E_r in Newton–HD. The results shown in this work have been calculated using the FP method, as we have verified that it is usually the fastest one with respect to the other two.

4. Benchmarks and Applications

In this section we show a series of tests of the code’s performance, paying special attention to the applicability of the RSLA in the context of protostellar disks. All of the results shown in this section are computed employing HLLC solvers for both the HD and radiation fields, using the third-order weighted essentially non-oscillatory (WENO) reconstruction scheme by Yamaleev & Carpenter (2009), and applying the IMEX1 scheme at the radiation step. Benchmarks where matter is either static or does not interact with radiation, such as the free streaming of beams, the formation of shadows, the transport of radiative pulses under different choices of coordinates, and the higher accuracy of our HLLC Riemann solver for radiation transport with respect to the HLL solver in Riemann problems, exhibit no differences with the results presented in Melon Fuksman & Mignone (2019), except for the fact that the velocity of freely streaming radiation is now replaced by \hat{c} . Hence, we do not show such tests in this work. Additional performance tests and comparisons with other works can be found in Appendix.

4.1. Radiative Shocks

We tested the code’s ability to reproduce shock waves in optically thick media, in which the dynamical evolution of

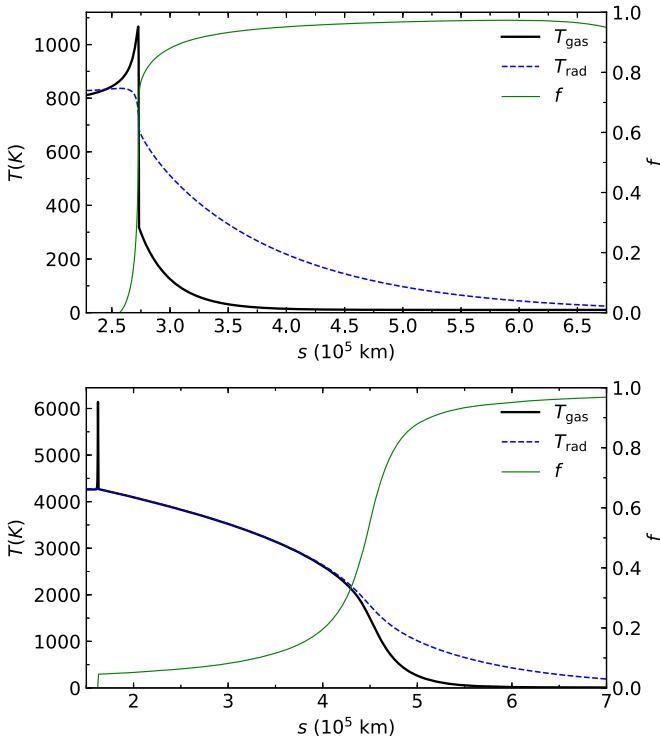


Figure 1. Gas and radiation temperature profiles, here denoted by T_{rad} and T_{gas} , for the subcritical (top) and supercritical (bottom) shock problems, shown, respectively, at $t = 3.8 \times 10^4$ and $t = 7.5 \times 10^3$ s as a function of $s = x - ut$. The reduced flux $f = \|\mathbf{F}_r\|/E_r$ is also shown to illustrate the transition between the streaming and the diffusion limits. The profiles have been computed with a resolution of 2400 zones in both cases.

matter and radiation fields is coupled. We reproduced the 1D setup considered in Ensmann (1994), which is generally used as a standard benchmark in Rad-HD codes (see, e.g., Hayes & Norman 2003; González et al. 2007; Commerçon et al. 2011; Kolb et al. 2013; Colombo et al. 2019). In this configuration, both matter and radiation fields are initially uniform in a domain given by the interval $[0, 7 \times 10^{10}]$ cm. The initial density is $\rho = 7.78 \times 10^{-10}$ g cm $^{-3}$, while the pressure and initial radiation fields are set in LTE at an initial temperature of $T_1 = 10$ K, with $\mu = 1$ and $\Gamma = 7/5$ (see Equations (5) and (11)). Opacities are set in such a way that $\kappa\rho = 3.1 \times 10^{-10}$ cm $^{-1}$, with $\sigma = 0$. A rightward-moving shock is generated by setting an initially negative velocity u , and imposing reflective conditions on the left boundary.

Radiative shocks are extensively studied, e.g., in Zel’dovich & Raizer (1967) and Mihalas & Mihalas (1984). In the general case, radiation escaping from the shock front will cause the pre-shock region to raise its temperature until reaching a value T_- at the shock front. In the shocked region, the temperature decreases from its maximum value T_+ at the shock front until its post-shock value T_2 . The behavior of the solutions depend of the fluid’s velocity, in our case parameterized by u . For values of $|u|$ below a critical value u_{cr} , the resulting temperature profile verifies $T_- < T_+$, and the produced shock is said to be *subcritical*. For higher velocities shocks are said to be *critical* if $|u| = u_{\text{cr}}$ and *supercritical* if $|u| > u_{\text{cr}}$, and always verify $T_- = T_+$.

We employed two values of u given by -6 and -20 km s $^{-1}$, which correspond respectively to subcritical and supercritical velocities. We produced numerical solutions starting from both conditions using in every case a uniform grid of 2048 zones,

setting $\hat{c} = c$ to avoid inaccuracies produced by the RSLA. These results are shown in Figure 1, in which we show the obtained temperature profiles at $t = 3.8 \times 10^4$ s and $t = 7.5 \times 10^3$ s for the subcritical and supercritical shock, respectively. We have as well computed the radiation temperature T_{rad} , defined as $T_{\text{rad}} = (E_r/a_R)^{1/4}$, which corresponds to the equilibrium temperature in LTE. In the same figure we have represented the reduced flux $f = \|\mathbf{F}_r\|/E_r$. All profiles have been plotted as a function of $s = x - ut$ for comparison with the mentioned works. The structure of the temperature in the precursor, namely the heated pre-shocked region, differs in both cases. In the subcritical shock there is an abrupt transition from the diffusion to the streaming limit. In the entire precursor, f remains above 0.75, and T_{rad} exceeds the gas temperature. This transition is much smoother in the supercritical shock, where $T_{\text{rad}} = T$ and $f \leq 0.3$ in a large portion of the precursor. We obtain $T_+ = 1067$ K, $T_- = 317$ K, and $T_2 = 812$ K for the subcritical shock, and $T_+ = 6140$ K and $T_2 = 4260$ K in the supercritical shock. In the first of these cases, all temperatures except T_2 exceed those obtained with FLD at the same resolution (see, e.g., Commerçon et al. 2011), and the same holds for T_+ in the second case. Differences can also be seen in the precursors, which have a generally larger spatial extent with the M1 closure than with FLD (see also González et al. 2007). It is not possible from this comparison to conclude that one of the two methods yields more accurate results in this particular case, as both of them rely on an approximate closure. In general, both methods produce similar results in 1D, whereas the M1 method outperforms FLD in multidimensional anisotropic setups, e.g., involving beams or shadows. A better comparison in this 1D case would require the employment of radiative transfer techniques that do not depend on the choice of a closure prescription (see, e.g., Davis et al. 2012), which is beyond the scope of this paper.

We used this test to study the limits of the RSLA formalism when applied to nonequilibrium systems. To do this, we have performed the same tests using different values of \hat{c} of the form $c/10^n$, with $n \in [0, 4]$. The resulting T and T_{rad} profiles are shown in Figure 2 at the same times as those in Figure 1. The obtained temperatures are systematically smaller than their values with $\hat{c} = c$ as \hat{c} is reduced as a result of the nonconservation of the total energy in the RSLA. Using the first of Equation (16) together with the condition $\Delta E_{\text{tot}} = 0$ verified in the implicit step (Equation (25)), we can write the variation of the total energy as

$$\Delta(E + E_r) = (1 - c/\hat{c})\Delta E_r, \quad (30)$$

which is negative unless $\hat{c} = c$, since $\Delta E_r > 0$ in this case. Therefore, more energy will be artificially lost for smaller values of \hat{c} . Since the conversion of kinetic energy into thermal energy is faster in the supercritical shock than in the subcritical shock, this effect is more important in the former, while the latter can be reproduced by the RSLA for smaller \hat{c} values. As an example, the relative L $_1$ -norm difference between the obtained T with $\hat{c} = c$ and $\hat{c}/1000$ is of 0.2% in the subcritical shock and 41% in the other case.

We can give rough estimates for the range of values of \hat{c} in which the RSLA is applicable by applying Equation (17) computing τ_{max} as the total optical depth of the domain and replacing v_{max} by the maximum value of $|v_x| + c_s$, where c_s is the fluid’s sound speed. Using the profiles obtained with $\hat{c} = c$,

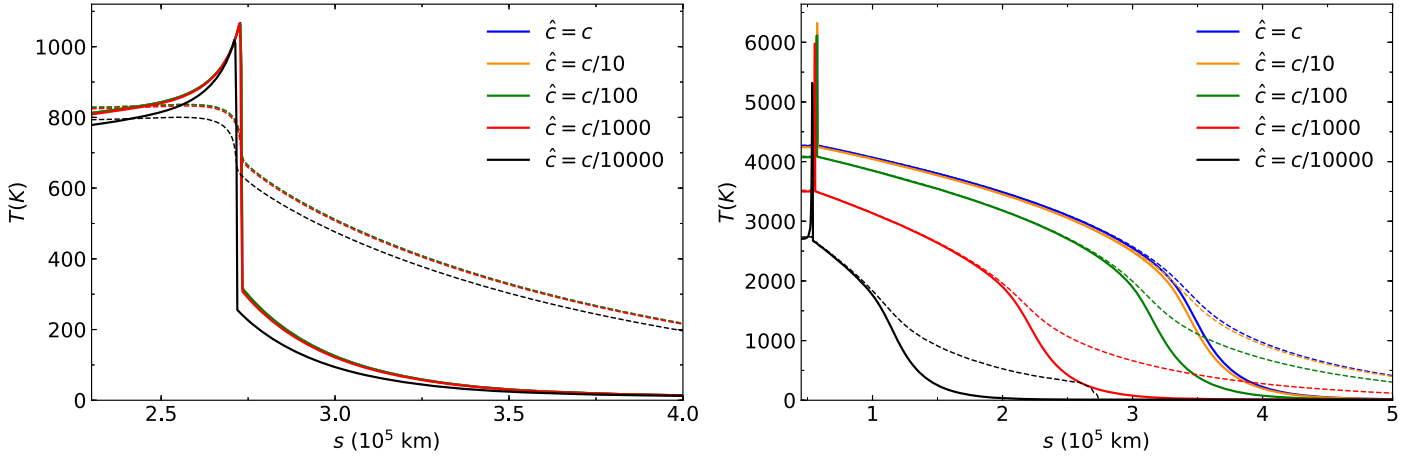


Figure 2. Gas (solid lines) and radiation (dashed lines) temperature profiles of the subcritical (left panel) and supercritical (right panel) shocks computed at a resolution of 2400 zones for different values of \hat{c} . The profiles are shown at the same times as those in Figure 1 as a function of $s = x - ut$.

this yields the conditions $\hat{c} \gg c/2068$ and $\hat{c} \gg c/543$ for the subcritical and supercritical shocks respectively. This criterion alone does not explain why in the subcritical case the solutions depart more than 1% from the $c = 1$ solution only for \hat{c} below its approximate limiting value, whereas in the supercritical case they do so for $\hat{c} = c/100$, which is still about five times larger than $c/543$. However, this timescale analysis does not contemplate the error introduced by the RSLA when gas energy is continuously injected into the system from the boundaries and converted into radiation energy, which can cause a significant energy loss for sufficiently low \hat{c} (see Equation (30)). To obtain an approximate condition for the validity of the RSLA in this case, we estimate the ratio of lost energy to total kinetic energy converted into internal energy at the left boundary as $\max(\Delta(E + E_r)/(\rho\epsilon + E_r))$, where we use Equation (30) to compute $\Delta(E + E_r)$ taking $\Delta E_r \approx E_r$. Requiring this ratio to be much smaller than 1 and approximating $1 - c/\hat{c} \approx -c/\hat{c}$, this gives the condition $\hat{c} \gg c/50,000$ for the subcritical shock and $\hat{c} \gg c/400$ for the supercritical shock. Therefore, errors above 1% can be seen in both shocks when \hat{c} is about four to five times larger than these limiting values. However, as is the case for Equation (17), these are approximate relations, and optimal values of \hat{c} are better determined in general through testing.

4.2. Diffusion in Disk Atmospheres

As a first application of the code in the context of protoplanetary disks, we have considered a one-dimensional setup representing a vertical slice of a disk at a radius $R = 5$ au with respect to a central star of mass M_\odot . We used this setup to test the effect of the RSLA on the timescales corresponding to processes of viscous heating and radiative diffusion. Similar tests have been performed e.g., in Zhu et al. (2020).

We define this problem in a domain given by the interval $[-1, 1]$ au, where we set a Gaussian density profile defined as

$$\rho(x) = \rho_0 \exp(-x^2/2H^2) + \rho_{\min}, \quad (31)$$

where $\rho_0 = 10^{-10}$ g cm $^{-3}$ and $\rho_{\min} = 10^{-10}\rho_0$, while the pressure scale height H is defined in such a way that $H/R = 0.05$. Such a distribution represents a vertical density profile resulting from the balance between the gravitational force of the star and the internal pressure of the disk. Since in this case we are solely interested in the diffusion of radiative

energy, we neglect gravity and all advection terms for energy-momentum and matter. The resulting evolution equations are therefore

$$\begin{aligned} \frac{\partial E}{\partial t} &= cG^0 + S_E \\ \frac{1}{\hat{c}} \frac{\partial E_r}{\partial t} + \frac{\partial F_r^x}{\partial x} &= -G^0 \\ \frac{1}{\hat{c}} \frac{\partial F_r^x}{\partial t} + \frac{\partial P_r^{xx}}{\partial x} &= -G^x. \end{aligned} \quad (32)$$

Following the α prescription by Shakura & Sunyaev (1973), we compute the viscous heating term as $S_E = \frac{9}{4}\alpha\Omega_K c_s^2 \rho$, where $\alpha = 10^{-3}$, Ω_K is the Keplerian angular velocity at 5 au, and c_s is the speed of sound computed at the initial uniform temperature $T_0 = 1000$ K. We set the absorption opacity $\kappa = 0.1$ cm 2 g $^{-1}$, zero scattering, $\mu = 2.35$, and an adiabatic index $\Gamma = 1.41$, corresponding to typical values for solar composition (Decampli et al. 1978). Initial LTE conditions with $T = T_0$ are imposed in the entire domain at $t = 0$ and at the boundaries for $t > 0$, while zero-gradient boundary conditions are imposed on F_r^x .

The final state of this system corresponds to a stationary configuration in which viscous heating and radiation diffusion are in equilibrium. This solution can be obtained semi-analytically by setting all time derivatives in Equation (32) to 0, which leads to $G^0 = -S_E/c$. Since S_E is a known function of x , the second of these equations can be numerically integrated to yield F_r^x , for which we use the condition $\partial_x F_r^x = 0$ at $x = 0$. The third equation can be in turn integrated to yield $P_r^{xx}(x)$ using the values of $E_r = a_R T_0^4$ and F_r^x at one of the domain boundaries. Lastly, the values of $P_r^{xx}(x)(E_r, F_r^x)$ can be inverted to obtain E_r . This inversion leads to unique E_r solutions provided $F_r^x/E_r < 3/7$ (Melon Fuksman & Mignone 2019), which is satisfied since in our case $F_r^x/E_r \sim 10^{-5}$.

Simulations have been run taking $\hat{c} = c/10$, $c/100$, and $c/1000$, at a resolution of 201 zones in each case. The resulting E_r and F_r^x profiles are shown in Figure 3 at $t = 3.8$ yr = $1.06 \Omega_K^{-1}$, together with the described semi-analytical solution, where a good agreement is obtained in each case.

In the right panel of Figure 3 we have plotted as a function of time the L_1 -norm relative difference between the numerical

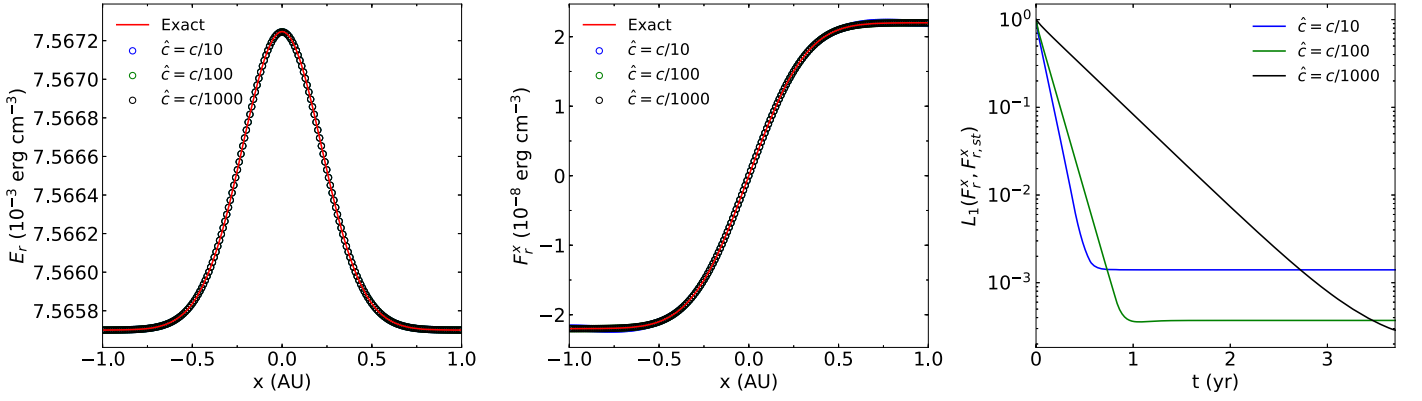


Figure 3. Left panel: radiation energy density at $t = 3.8$ yr in the diffusion test for different values of \hat{c} , compared with the exact semi-analytical stationary solution. Middle panel: same as the plot in the left panel, this time showing the equilibrium radiative flux. Right panel: relative L_1 -norm difference between the numerical and analytical values of F_r^x as a function of time.

values of F_r^x and the stationary semi-analytical solution. We can see in that figure that the stationary solution is reached at earlier times for larger \hat{c} and that smaller \hat{c} values lead to more accurate stationary solutions. The reason for this is that a slower evolution of the system leads to smaller values of the time derivatives, which reduces the imbalance between cG^0 and S_E caused by operator splitting error. We estimated the timescale in which the radiative flux reaches its final configuration by computing the initial slopes of these curves, obtaining $t_{\text{eq}} = 0.045 \Omega_K^{-1}$, $0.062 \Omega_K^{-1}$, and $0.224 \Omega_K^{-1}$ for $\hat{c} = c/10$, $c/100$, and $c/1000$, respectively.

4.3. Convective Instability in Protoplanetary Disks

We now turn to a scenario in which convective vertical flows are spontaneously produced in a protoplanetary disk. Convection occurs when vertical superadiabatic temperature gradients are created, which in our case happens as a product of the balance between viscous heating, adiabatic compression, and radiative diffusion in the disk. Such unstable temperature gradients are difficult to sustain in time, as reviewed in Klahr (2007), and it is unknown whether they can be maintained through some support mechanism such as the formation of strong spiral shocks caused by orbiting planets (Lyra et al. 2016). However, convective energy transport might still regulate the formation of vertically adiabatic stratifications, which aids the growth of other turbulence-driving mechanisms such as the vertical shear instability (see Pfeil & Klahr 2019). Therefore, vertical convection might still have a role in the development of turbulence and angular momentum transport in the dead zones of protoplanetary disks, where the low ionization degrees render the magnetorotational instability inefficient (Gammie 1996).

We applied our code to describe a convectively unstable setup, with a particular focus on how the RSLA affects the evolution of the instability. We consider the case of an axisymmetric disk, and solve the Rad-HD equations in a 2D grid using spherical coordinates (r, θ) . Similar configurations have been considered in Cabot (1996) and Klahr et al. (1999). This time we solve the full Rad-HD equations, including the viscous heating source terms given by Equation (9) and the gravitational potential of a solar mass star, given by $\Phi(r) = -GM_\odot/r$. We set an initial vertically isothermal configuration at LTE, with the density and rotational angular

velocity given by

$$\rho(R, z) = \rho_0 \left(\frac{R}{R_0} \right)^p \exp \left(\frac{R^2}{H^2} \left[\frac{R}{\sqrt{R^2 + z^2}} - 1 \right] \right)$$

$$\Omega(R, z) = \Omega_K \left[(1 + q) - \frac{qR}{\sqrt{R^2 + z^2}} + (p + q) \frac{H^2}{R^2} \right], \quad (33)$$

(see, e.g., Fromang et al. 2011), where $(R, z) = (r \sin \theta, r \cos \theta)$ are the cylindrical radius and height, while $\rho_0 = 10^{-9} \text{ g cm}^{-3}$, $R_0 = 1 \text{ au}$, $p = -2$, $q = -1/2$, and $\Omega_K = \sqrt{GM_\odot/R^3}$ is the midplane Keplerian angular velocity. The pressure scale height is computed as $H = H_0(R/R_0)^{(q+3)/2}$, where $H_0/R_0 = 0.035$. With the chosen value of q , this gives an increasing H/R ratio proportional to $R^{1/4}$. The gas pressure is computed as $p_g = \rho c_s^2$, where c_s is the local sound speed, estimated as $c_s = H\Omega_K$. In this way, the initial temperature decreases radially as $T \propto R^q$.

Accretion disks are unstable to thermal vertical convection under the condition that entropy decreases away from the disk midplane, i.e.,

$$\frac{\partial S}{\partial |z|} = C_v \frac{\partial}{\partial |z|} \log \left(\frac{p_g}{\rho^\Gamma} \right) < 0, \quad (34)$$

where S is the specific entropy and C_v is the specific heat at constant volume. Lin & Papaloizou (1980) have shown that such a gradient can be obtained in a disk that radiates vertically while decreasing its internal energy and consequently shrinking. Considering an absorption opacity of the form $\kappa = \kappa_0 T^\beta$, they derived the criterion

$$\frac{1}{4 - \beta} \geq \frac{\Gamma - 1}{\Gamma} \quad (35)$$

for the disk to be vertically unstable to convection. For our model, we have used the absorption opacity law by Bell & Lin (1994), which consists of a series of broken power laws of the form $\kappa = \kappa_0 \rho^\alpha T^\beta$ corresponding to the absorption of millimeter-sized grains in different temperature regimes. For temperatures of at most a few hundred Kelvin the absorption opacity is dominated by ice grains if $T \lesssim 160 \text{ K}$, in which case $\kappa_0 = 2 \times 10^{-4} \text{ cm}^2 \text{ g}^{-1}$, $\alpha = 0$, and $\beta = 2$, while for higher temperatures metal grains dominate the absorption, and the parameters are $\kappa = 0.1 \text{ cm}^2 \text{ g}^{-1}$, $\alpha = 0$, and $\beta = 1/2$. For

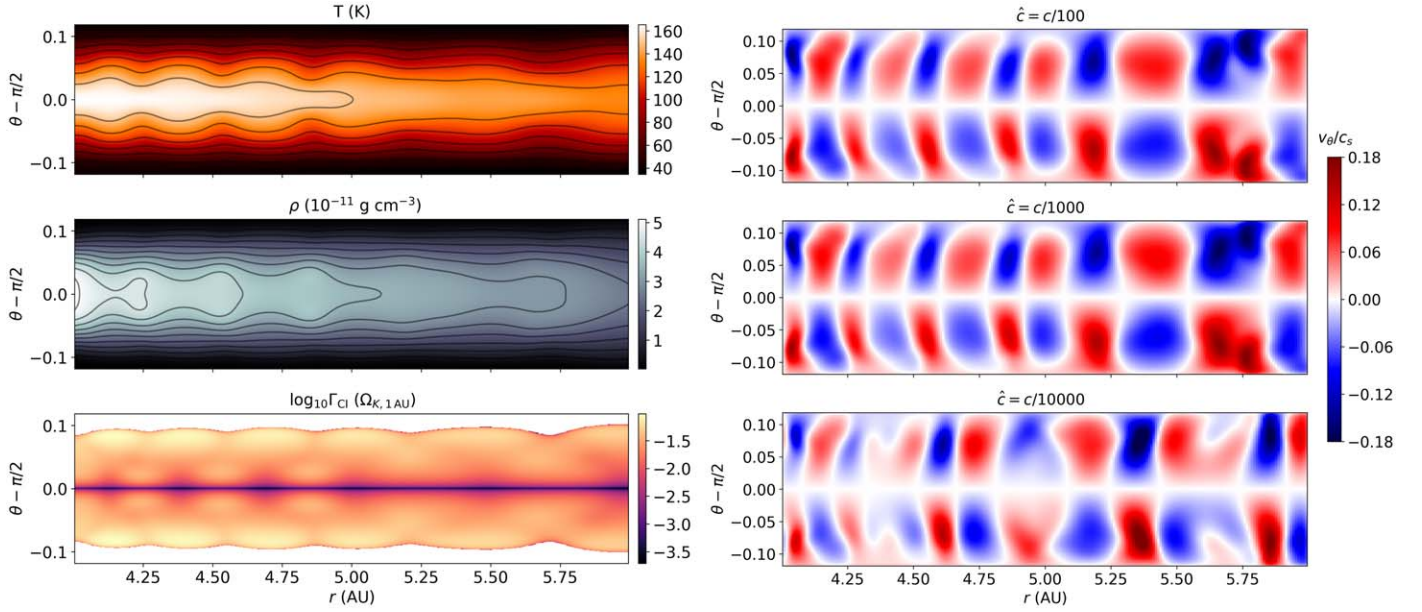


Figure 4. Left panel: temperature (upper panel), density (middle panel), and logarithm of the growth rate of the convective instability (lower panel) as a function of (r, θ) in run C3, plotted at $t = 200 T_0$. Contour lines are included in the temperature profile every 20 K between 50 and 160 K, as well as in the density profile every 0.5 g cm^{-3} between 0 and 5 g cm^{-3} . Right panel: values of v_θ/c_s after 200 orbits in runs C2, C3, and C4.

$\Gamma = 1.41$, we obtain that condition (35) is only satisfied below the ice line. For this reason, we have chosen our parameters in such a way that the temperatures do not overpass this threshold, but remain high enough that a superadiabatic temperature gradient is produced before all energy is radiated away. We also set zero scattering and $\mu = 2.35$.

In order to satisfy these conditions, we model the disk in the region $(r, \theta) \in [4, 6] \text{ au} \times [\pi/2 - 0.12, \pi/2 + 0.12]$, with a viscosity determined by the α prescription (Shakura & Sunyaev 1973) as $\nu = \alpha \Omega_K^{-1} p_g / \rho$ (see Equation (10)). We impose zero-gradient conditions for p_g in the inner and outer radial boundaries, setting $v_\phi = \Omega R$ as in Equation (33) and $v_r = v_\theta = 0$, in such a way that the mass flow through these boundaries is zero. In the poloidal direction reflective conditions are applied on all HD fields. We set the radiation flux to zero gradient except in the case of radiation inflow, in which case impose reflective conditions. The radiation energy is set to zero gradient in the radial direction, whereas in the poloidal direction we fix it to $E_r = a_r T_{\min}^4$ with $T_{\min} = 10 \text{ K} \ll T$ in all ghost cells. This is essential to ensure that the radiated energy leaves the system instead of accumulating in the domain, eventually leading to the thermalization of the system.

Computations have been run on a grid of 256^2 zones logarithmically spaced in the radial direction, using $C_a = 0.3$ for both the radiation and HD fields. We performed three different runs of this test using in each case a different value of \hat{c} , namely $\hat{c} = c/100$, $c/1000$, and $c/10,000$. We refer to these simulations as C2, C3, and C4, respectively. We ran C2 and C4 for a total of 275 orbits and C3 for 500 orbits, where we define an orbit as the Keplerian period at 1 au, i.e., $T_0 = 2\pi/\Omega_{K,1 \text{ au}}$.

In every run, the system goes through an initial relaxation phase lasting a few tenths of orbits, in which radially oriented sound waves can be observed in the velocity profiles. The entropy gradient becomes unstable close to both vertical boundaries from the first orbit. The unstable regions migrate toward the midplane until merging at $t \approx 70 T_0$. At this point,

vertical convective cells can begin to be observed in the velocity profile, and at $t \approx 100 T_0$ they become evident in the density and temperature profiles as well. This can be seen in Figure 4, where we have plotted the temperature and density profiles in run C3 at $t = 200 T_0$. In the same figure we have plotted v_θ/c_s , i.e., the projection of the velocity onto \hat{e}_θ normalized by the local sound speed. In this case the profile evidences a series of radially distributed expansive and compressive zones. The temperature profile has a larger scale height in the expansive zones, and vice versa, whereas the density scale height is larger in the compressive ones. Convection cells continuously migrate in the radial direction, interacting with each other and sometimes merging.

We can see in the v_θ/c_s profiles that convective cells occupy almost the entire domain, with a vertical size limited by the size of the domain, and a typical radial extension of about a pressure scale height, here roughly 0.1–0.3 au. In C2 and C3 the average maximum v_θ/c_s is 0.26, whereas in C4 this value is reduced to 0.19. We compare the velocity profiles at 200 orbits in Figure 4, where it can be seen that the profiles in C2 and C3 are almost identical, while differences can be observed with respect to C4.

The computed vertical velocities can be used to verify the constraint on the value of \hat{c} given by Equation (17). Using the maximum values of v_θ in C2 as v_{\max} and computing the vertical optical depth from the disk midplane, we obtain the constraint $\hat{c} \gg c/8000$, which is not satisfied by C4. In C3, on the other hand, the value of \hat{c} exceeds the limit value by a factor 8.

The unstable region of the domain is shown in Figure 4 at 200 orbits in C3. In the same figure we have indicated the growth rate of the instability at each position, calculated in terms of the vertical Brunt–Väisälä frequency N_z (see, e.g., Rüdiger et al. 2002) as

$$\Gamma_{\text{CI}} = \sqrt{-N_z^2} = \sqrt{\frac{1}{\Gamma \rho} \frac{\partial p_g}{\partial z} \frac{\partial}{\partial z} \log \left(\frac{p_g}{\rho^\Gamma} \right)}. \quad (36)$$

We see that the unstable region occupies the entire radial extension of the domain and almost its entire angular extension.

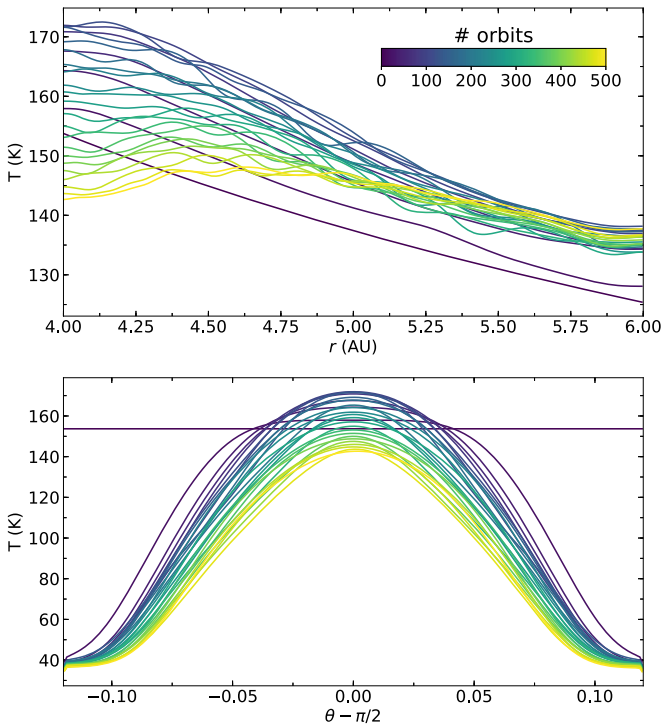


Figure 5. Temperature profiles in run C3 at $\theta = \pi/2$ (top panel) and $r = 4$ au (bottom panel), plotted every 20 orbits. The color scale indicates the current number of orbits for each profile.

The growth rate increases for larger heights at each r , reaching at that time a maximum value of of $9.7 \times 10^{-2} T_0^{-1}$.

In Figure 5 we show two series of 1D temperature profiles, one of them at $r = 4$ au and the other one at $\theta = \pi/2$, computed in C3 every 20 orbits. The disk midplane goes through an initial heating phase that lasts approximately 100 orbits, reaching a maximum temperature of ~ 170 K at $r = 4$ au. During this phase, the outer boundaries of the disk begin to radiate out internal energy, steepening the vertical temperature gradient until it becomes unstable and triggers the convective motion. Approximately at that time, the midplane temperature profile begins to flatten as the internal energy of the higher-temperature regions escapes the system through radiative diffusion. At $t = 500 T_0$, convection is still occurring and the disk is steadily cooling down while the unstable region slowly begins to shrink.

Throughout the disk evolution, momentum and entropy are vertically transported through convection. To measure the vertical entropy transport, we define the convective heat flux at a given θ as

$$j_E(t, \theta) = \langle \epsilon'(\rho v_\theta)' \rangle_r, \quad (37)$$

where $\langle \cdot \rangle_r$ represents average in r , and primed quantities correspond to deviations with respect to the average, i.e.,

$$v'(t, r, \theta) = v(t, r, \theta) - \langle v \rangle_r(t, \theta), \quad (38)$$

where v is any given field. The behavior of j_E as a function of time is oscillatory, as can be seen in Figure 6, where we have plotted j_E in run C3 as a function of θ every 10 orbits from 100–270 orbits. It can already be seen in this figure that transport occurs predominantly outwards. This can be quantified in a more precise way by computing the time average of j_E , which we denote as $\langle j_E \rangle_r$. In Figure 6 we show these averages

between 100 and 270 orbits for all runs. We obtain similar functions for C2 and C3, whereas in C4 the maximum flux is reduced to approximately to 50% of its value in C2 and C3.

The above results show that convective energy transport becomes more inefficient when the speed of light is reduced. Naturally, the same happens with the radiative energy transport. To compare the effect of the reduction of \hat{c} on both mechanisms, we have quantified the ratio between convective and radiative energy transport analog to Bell et al. (1997) in the spirit of a Nusselt number, defined in this case as

$$\text{Nu}_\theta(\theta, t) = \frac{j_E}{\langle F_r^\theta \rangle_r}. \quad (39)$$

Note that the classical Nusselt number gives the enhancement factor of total heat transport if convection adds to conduction, which can never be smaller than 1. As we do not determine the heat transport for the radiation transport only case, we slightly modified our definition of Nu_θ as ratio of conductive transport over radiation transport, while both are active, and thus our Nu_θ can obtain values of less than one. We computed the time-averaged value of Nu_θ for all runs, shown in Figure 6. We observe differences in $\langle \text{Nu}_\theta \rangle_t$ close to its maximum value, which tends to decrease for increasing \hat{c} . We obtain $\max \langle \text{Nu}_\theta \rangle_t = 0.39$ in C2, 0.38 in C3, and 0.34 in C4. We conclude that the RSLA can reproduce the main features of this model for $\hat{c} \geq c/1000$.

4.4. Planet–disk Interaction

We now present an application of the code in the context of giant planet formation. The most widely accepted explanation for this phenomenon is the core accretion scenario, in which giant planets form as a consequence of gas accretion by large ($\gtrsim 10 M_\oplus$) planetary cores in protoplanetary disks (Mizuno 1980; Bodenheimer & Pollack 1986; Pollack et al. 1996). The momentum exchange caused by the gravitational influence of the protoplanet produces spiral waves in the disk, and if the planet is sufficiently massive, i.e., if its Hill radius exceeds the pressure scale height of the disk, it can lead to the formation of annular gaps (see, e.g., Kley & Nelson 2012). These structures are affected by the thermal structure in the disk, which consequently affects key properties for the planet’s evolution such as its migration and accretion rates. In particular, the low densities produced during the formation of gaps may produce transport of radiation from optically thick to optically thin regions, for which the M1 closure is particularly suited.

We applied our scheme to describe the accretion process onto a gap-opening planet embedded in a protoplanetary disk. Similar studies have been carried out, e.g., in Klahr & Kley (2006), Ayliffe & Bate (2012), and Schulik et al. (2019). We consider a disk around a solar mass star, in which a planet of mass $M_p = M_J$ orbits at a radius $r = 5$ au. We define this setup in a 3D domain given in spherical coordinates as $(r, \theta, \phi) \in [3, 7.5] \text{ au} \times [\pi/2 - 0.12, \pi/2 + 0.12] \times [0, 2\pi]$, where $r = 0$ corresponds to the center of mass of the planet–star system. The gas distribution is defined in the same way as in Section 4.3, where this time $H_0/R_0 = 0.05$, $p = -3/2$, and $q = -1$. In this way, the disk has an initially uniform H/R ratio, and the vertical domain exceeds the pressure scale height by a factor 2.4. In this case, no viscosity is included. Boundary conditions remain the same as in Section 4.3, with the difference that now

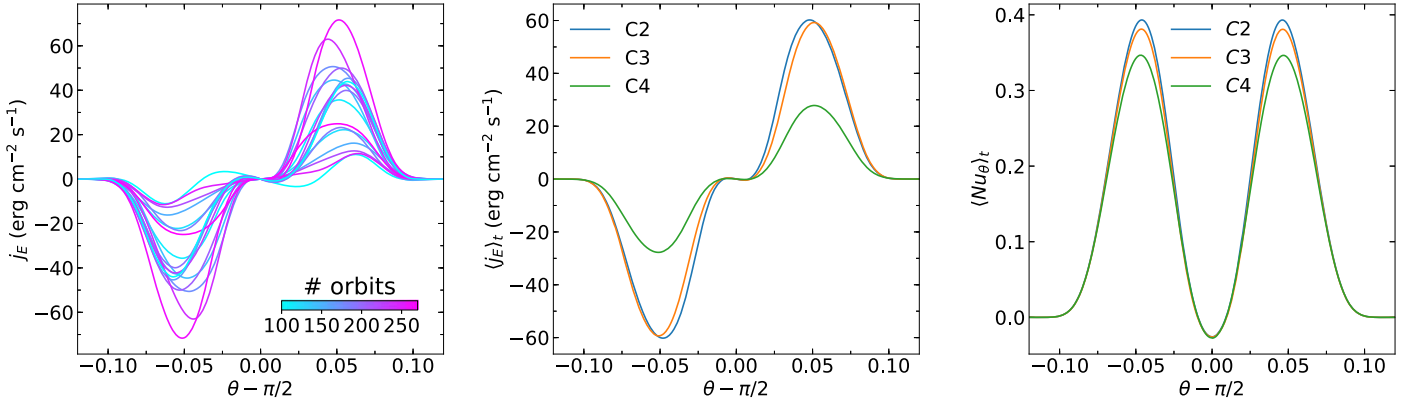


Figure 6. Left panel: vertical convective heat flux j_E as a function of time, plotted every 10 orbits between 100 and 270 orbits. Middle panel: time-averaged j_E profiles for runs C2, C3, and C4. Right panel: time-averaged Nusselt number for the same runs.

we apply zero-gradient conditions for E_r in the vertical boundaries and periodic conditions to all variables in the azimuthal direction.

The total gravitational potential is computed as a sum of the potentials Φ_s and Φ_p due to the star and the planet. The stellar potential is computed as

$$\Phi_s = -\frac{M_\odot G}{\|\mathbf{r} - \mathbf{r}_s\|}, \quad (40)$$

where \mathbf{r}_s is the star's position. Following Klahr & Kley (2006), we compute Φ_p as

$$\Phi_p(\mathbf{r}) = \begin{cases} -\frac{M_p G}{d_p} & \text{if } d_p \geq a_g \\ -M_p G \left[\frac{d_p^3}{a_g^4} - 2\frac{d_p^2}{a_g^3} + \frac{2}{a_g} \right] & \text{if } d_p < a_g, \end{cases} \quad (41)$$

where $d_p = \|\mathbf{r} - \mathbf{r}_p\|$, \mathbf{r}_p is the planet's location, and a_g is a critical distance used to smooth the potential in the vicinity of the planet. We compute this quantity as $a_g = r_h/2$, where r_h is the planet's Hill radius, i.e., the approximate radius of its Roche lobe. This quantity can be computed in terms of the reduced mass of the system $\mu_p = \frac{M_p}{M_p + M_s}$ as

$$r_h = r_p \left(\frac{\mu_p}{3} \right)^{1/3}, \quad (42)$$

where r_p is the distance between the planet and the star. The planet's mass is smoothly incremented during the first orbit from 0 to M_p , in order to guarantee a slow adaptation of the system and prevent the formation of strong waves caused by an initial nonequilibrium configuration. In this work we do not include a local reduction of the density per time step in the vicinity of the planet accounting for the accretion, and focus solely on the heating and cooling caused by radiation transport.

We solve the Rad-HD equations in spherical coordinates on a grid with resolution $N_r \times N_\theta \times N_\phi = 128 \times 60 \times 512$, using $C_a = 0.3$ for both radiation and HD fields and $\hat{c} = c/1000$. The grid is logarithmically spaced in the radial direction and linearly divided in the azimuthal direction using two regions of different resolution, in such a way that the intervals $[0, \pi/2]$ and $[\pi/2, 2\pi]$ have each a resolution of 256 zones. We integrate these equations in a reference frame that

corotates with the planet, in such a way that the coordinates of the latter are always $(r_p, \theta_p, \phi_p) = (5 \text{ au}, \pi/2, \pi/4)$. This reduces the numerical diffusion around the planet, at the cost of integrating the extra few terms that arise when the HD equations are transformed into this frame. As mentioned in Section 2.1, in doing so we neglect all additional terms arising from the transformation of the radiation fields into the rotating frame, which is justified since $\Omega_p r_p/c \sim 10^{-5}$, where Ω_p is the Keplerian angular velocity of the planet.

We have run several tests with this configuration, neglecting scattering and using in each case $\kappa = \kappa_{\text{BL}}, \kappa_{\text{BL}}/100$, and $\kappa_{\text{BL}}/1000$, where κ_{BL} is the Rosseland opacity by Bell & Lin (1994) used in Section 4.3. We refer to these simulations as DP_K1, DP_K100, and DP_K1000, respectively. For comparison, we have also run a purely hydrodynamical test with the same initial setup. We refer to this run as DP_HD. We ran DP_K1 and DP_K1000 for a total of 5.5 orbits, where this time we define an orbit as the Keplerian period T_0 at the planet's location, while tests DP_HD and DP_K100 have been run for a total of 40 orbits.

In Figures 7 and 8 we show, respectively, vertical and horizontal slices showing the logarithms of ρ, T, E_r , and f at the planet's location, taken at $t = 5.5 T_0$. Since in run DP_HD we include no radiation, the E_r values shown in these figures for that test correspond to the LTE value given by $E_r = a_R T^4$. We did not compute an f value for that simulation. In each case we overplotted the location of the Hill sphere, i.e., the sphere of radius r_h centered on the planet, which approximates the outer boundary of the planet's Roche lobe.

These profiles evidence the formation two spiral arms, together with a hot gas envelope surrounding the planet that rotates in the same direction as it. The spirals are hotter than the surrounding material and colder than the central envelope. Profiles obtained in DP_HD and DP_K1 are almost identical, since for high opacities the LTE limit is recovered. These structures change and the overall temperatures decrease for lower opacities, as the radiation begins to diffuse away from the envelope and the spirals. Within the Roche lobe, the maximum temperature decreases for lower opacities from 543 K in DP_K1 (581 K in DP_HD) to 280 K in DP_K1000.

Similar changes can be observed in the E_r profiles, which show the same structure as the temperature profiles in DP_HD and DP_K1, whereas for lower opacities the energy density begins to fill the region surrounding the planet and the spiral arms. To see the direction of the radiative flux, we have

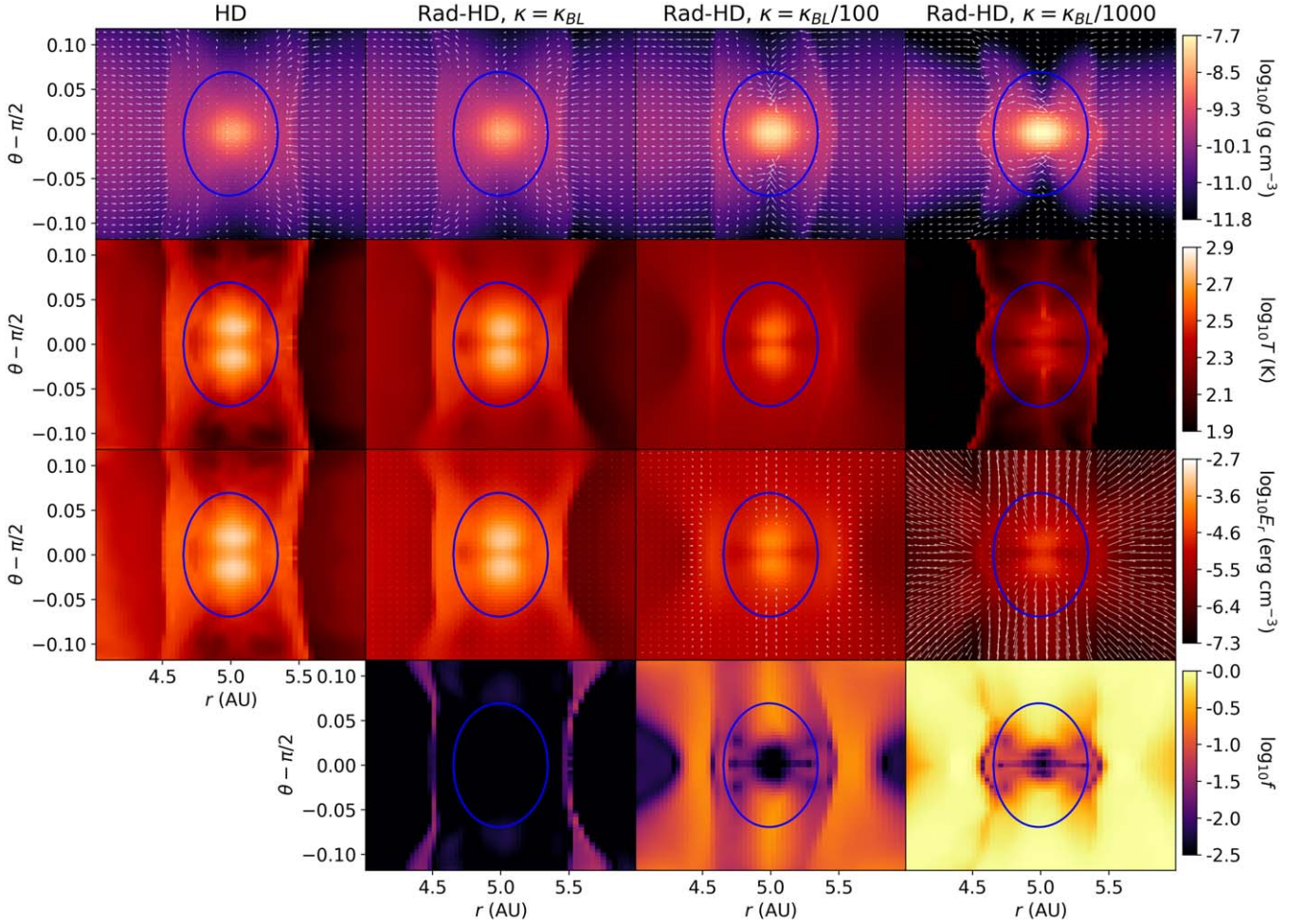


Figure 7. Vertical slices at the planet’s location in the planet–disk interaction test, shown at 5.5 orbits. From top to bottom, the logarithms of mass density, gas temperature, radiation energy density, and reduced radiative flux are represented in color scale. From left to right, the results are shown for runs DP_HD, DP_K1, DP_K100, and DP_K1000. The blue curve indicates in each case the location of the planet’s Hill sphere. White arrows representing the velocity field are superimposed in the density plots, where we have used the same scale for all runs. In the same way, the poloidal components of $f = F_r/E_r$, are represented in the E_r plots for DP_K1, DP_K100, and DP_K1000, using in each case the same scale.

superimposed in these profiles white arrows representing the value of $f = F_r/E_r$, using the same scale for every run. Together with the f plots, these profiles evidence the different regimes of radiation transport in the different runs. In DP_K1 the value of f remains below 0.07, and radiation is entirely in the diffusion regime. In DP_K100 we begin to see radiation transported away from the spiral arms with a maximum f of 0.25. On the other hand, the vertical slices show vertical transport of radiation at a maximum f of 0.14 through the low-density regions above and below the planet, which were caused by the planet’s gravitational attraction. Run DP_K1000, on the other hand, shows a transition between the diffusion regime, observed within the envelope and the spirals, and the almost freely transport streaming away from the spirals and in the vertical direction, with maximum $f = 0.94$. At this time, the radial optical depth across the Hill sphere is approximately 28,400, 690, and 150 in DP_K1, DP_K100, and DP_K1000, respectively, whereas the vertical optical depth across the Hill sphere in each of these cases is 19,000, 420, and 50. In DP_K100 and DP_K1000, the observed radiative losses occur despite these high values since most of this optical depth is caused by the large accumulation of mass close to the planet’s location, whereas diffusion is still possible around this region.

At $t = 0$, the radial optical depths across the same region are 3040, 30, and 3 in DP_K1, DP_K100, and DP_K1000, respectively, while the vertical ones are 2100, 21, and 2.

For decreasing opacities, the lower pressure support caused by radiation diffusion allows for a larger infall of matter onto the planet. This produces larger maximum densities in the envelope and also lower densities above and below the planet, as shown in the top rows of Figures 7 and 8. At that time, maximum densities range from $3.8 \times 10^{-9} \text{ g cm}^{-3}$ in DP_K1 ($3.5 \times 10^{-9} \text{ g cm}^{-3}$ in DP_HD) to $2.1 \times 10^{-9} \text{ g cm}^{-3}$ in DP_K1000. In the same plots, we have overplotted with white arrows the gas velocity in the planet’s corotating frame, using the same scale for every run. In the vertical profiles, it can be seen that matter is transported into the envelope predominantly from the poles, with maximum vertical mass fluxes ranging from $1.58 \times 10^{-5} \text{ g cm}^{-2} \text{ s}^{-1}$ in DP_K1 ($1.46 \times 10^{-5} \text{ g cm}^{-2} \text{ s}^{-1}$ in DP_HD) to $1.24 \times 10^{-4} \text{ g cm}^{-2} \text{ s}^{-1}$ in DP_K1000. In the horizontal profiles, we notice that conservation of angular momentum in the envelope causes the latter to rotate faster for decreasing opacities, with maximum angular velocities corresponding to rotational periods of 515 days in DP_K1 (655 days in DP_HD) and 186 days in DP_K1000.

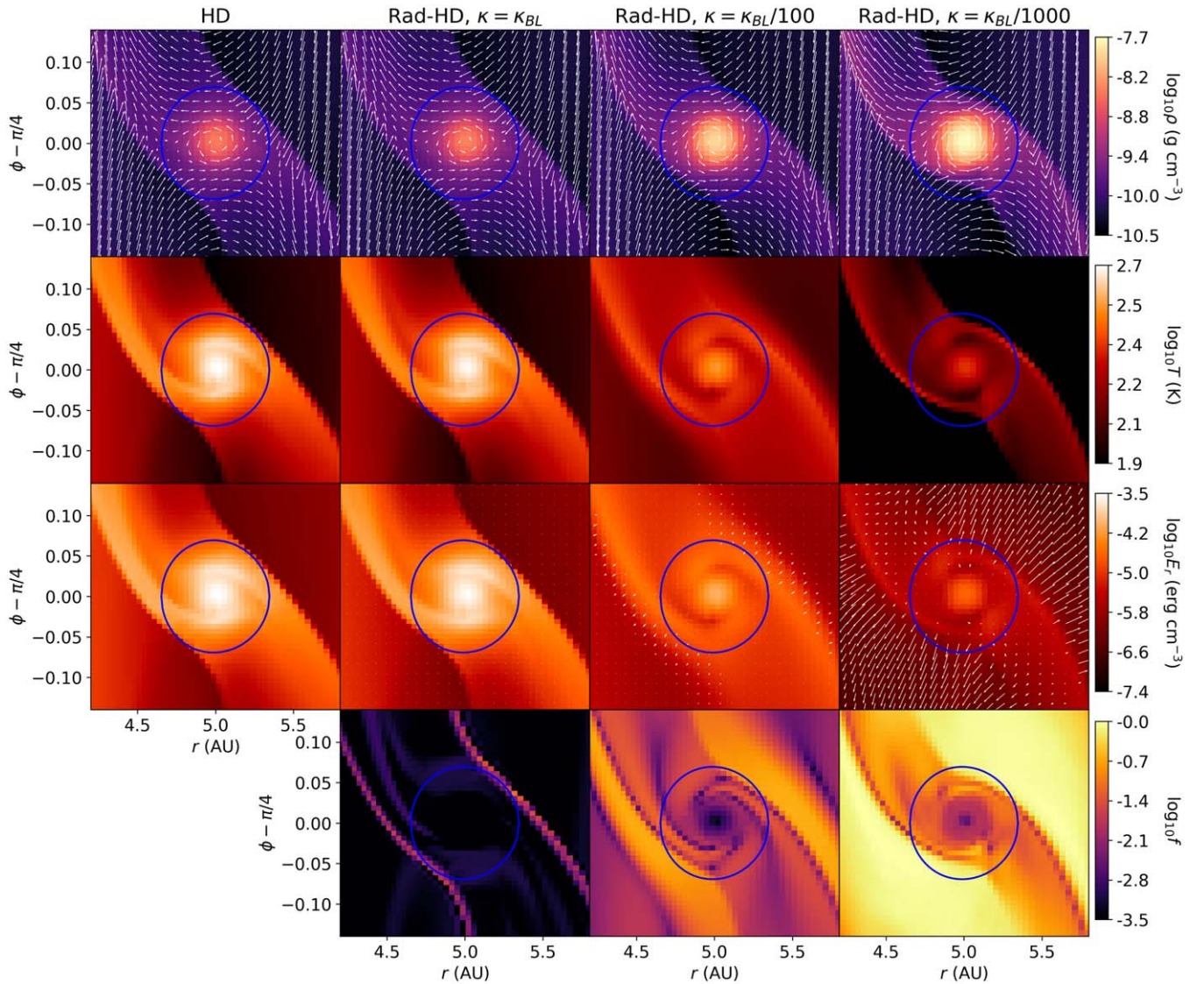


Figure 8. Same as Figure 7, this time showing horizontal slices of the represented fields at the planet’s location.

In Figure 9 we show (r, ϕ) profiles at $z = 0$ for runs DP_HD and DP_K100 after 40 orbits. Again, we observe lower temperatures and larger maximum densities close to the planet in DP_K100. We can see that the temperature distribution is much more uniform in DP_K100 than in DP_HD, where the temperature decreases in a neighborhood of the planet radius in the entire domain. We also notice structural differences in the gas density distribution, where matter within the planet’s horseshoe orbit has a lower density in DP_K100 than in DP_HD. This can be clearly seen in Figure 10, in which we show the gas density along the radial and azimuthal directions at the planet’s location. The first of these plots shows that the density in DP_K100 is larger than in DP_HD away from the planet except at a distance of $\sim 2r_h$ from the planet’s location, where the density in DP_K100 presents a sharp decrease unobserved in DP_HD. It is likely in this case that the vertical shrinking of the disk caused by radiative diffusion favors a faster formation of a gap at $r \sim 5$ au when compared to DP_HD.

We computed as a function of time the total mass M_{Hill} within the Hill sphere in both simulations, shown in Figure 11. In run DP_K100, M_{Hill} exceeds its value in DP_HD from the first orbit, reaching after 40 orbits $0.088 M_J$ in DP_K100 and $0.026 M_J$ in DP_HD. This shows that reducing the opacity would lead in this case to a faster growth of the planet. Similar conclusions are reached, e.g., in Movshovitz et al. (2010) and Schulik et al. (2020). We intend to carry high-resolution studies of this problem in the near future, using better estimates for the Rosseland and Planck opacities and including the mass decrease caused by accretion onto the planet.

4.5. Stellar Irradiation

We tested the implementation of the irradiation terms by reproducing the benchmark by Pascucci et al. (2004), which consists in computing the equilibrium temperature of a static disk irradiated by a central star. We compared temperature distributions obtained with both the presented module and the Monte Carlo radiative transfer code RADMC-3D (Dullemond et al. 2012).

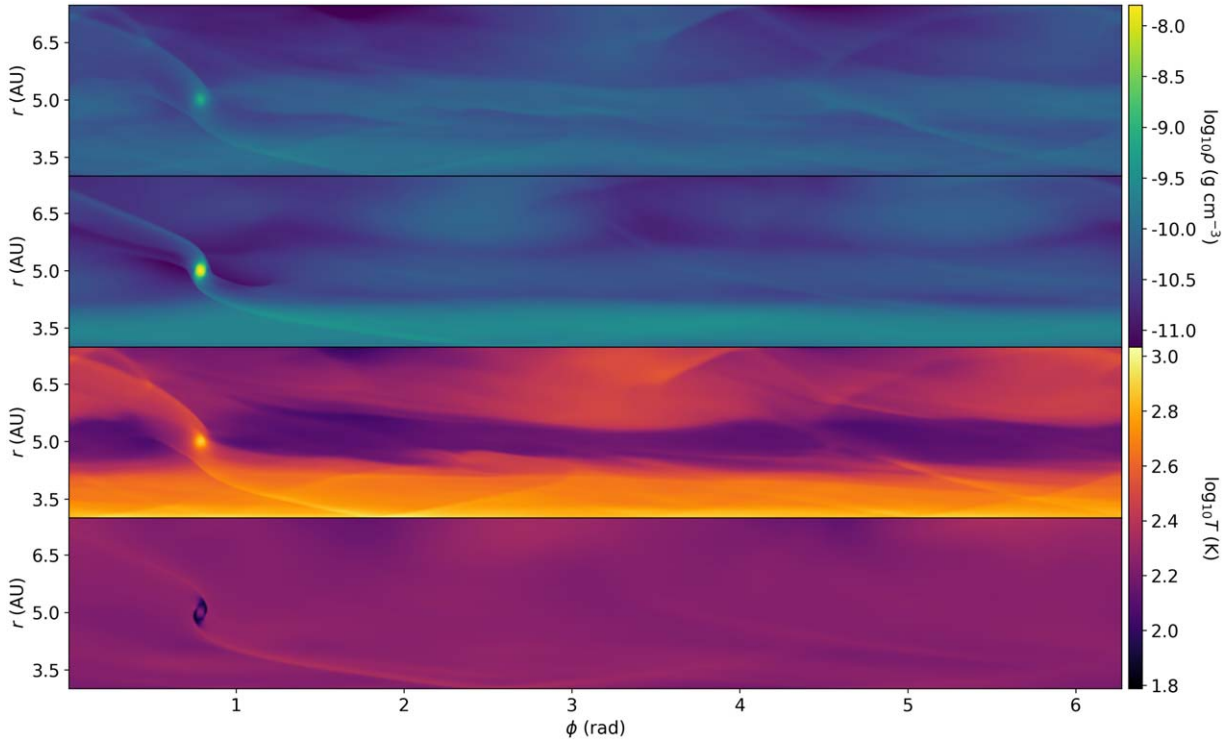


Figure 9. Horizontal (r, ϕ) slices in the planet–disk interaction test at 40 orbits. From top to bottom: $\log_{10} \rho$ for runs DP_HD and DP_K100, and $\log_{10} T$ for runs DP_HD and DP_K100.

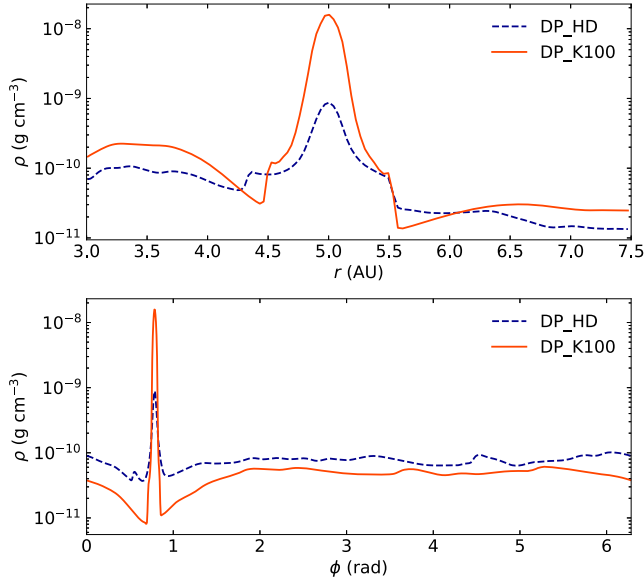


Figure 10. 1D mass density profiles at 40 orbits in runs DP_HD and DP_K100, computed as a function of r for fixed $\phi = \phi_p$ and $\theta = \theta_p$ (top panel), and as a function of ϕ for fixed $\theta = \theta_p$ and $r = r_p$ (bottom panel).

In both cases, the gas density is defined in spherical coordinates $(r, \theta) \in [1, 1000] \text{ au} \times [0, \pi]$ as

$$\rho(R, z) = \rho_0 \left(\frac{500 \text{ au}}{R} \right) \exp \left(-\frac{\pi}{4} \left(\frac{z}{h(r)} \right)^2 \right), \quad (43)$$

where $(R, z) = r(\cos \theta, \sin \theta)$ and $h(R) = 125 \text{ au} \times (R/500 \text{ au})^{1.125}$. To compute the opacities for both irradiation and radiation–matter interaction terms, we use the frequency-dependent absorption cross sections by Draine & Lee (1984),

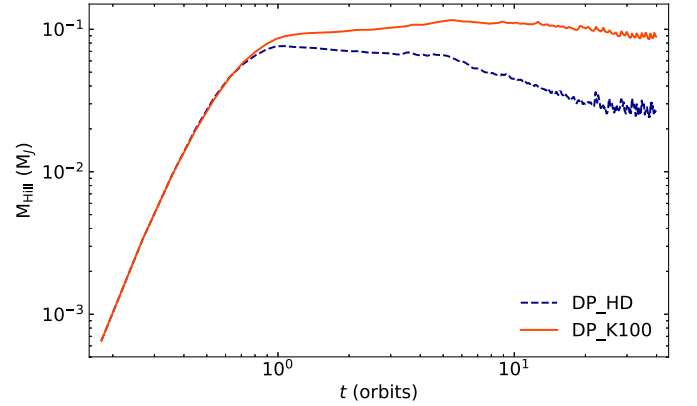


Figure 11. Mass enclosed in the Hill sphere in runs DP_HD and DP_K100 as a function of time.

derived for silicate dust particles with sizes between 0.003 and $1 \mu\text{m}$. To convert the tabulated cross sections into opacity coefficients, we assume the dust grains to have a radius of $0.12 \mu\text{m}$ and a density of 3.6 g cm^{-3} . We set $\rho_0 = 6.66 \times 10^{-17} \text{ g cm}^{-3}$ and a uniform dust-to-gas mass ratio of 0.01, in such a way that the absorption optical depth at 550 nm for a radial path that crosses the domain along the midplane equals $\tau = 100$.

In the Rad-HD simulation, the irradiation flux is computed as

$$F_{\text{irr}}(r, \theta) = \pi \left(\frac{R_s}{r} \right)^2 \int_{\nu_{\min}}^{\nu_{\max}} d\nu B_\nu(T_s) e^{-\tau(r, \theta, \nu)} \hat{\mathbf{r}}, \quad (44)$$

where $T_s = 5800 \text{ K}$ is the star temperature, $R_s = R_\odot$ is the star radius, $B_\nu(T_s)$ is the Planck radiative intensity, and $[\nu_{\min}, \nu_{\max}] = [1.5 \times 10^{11}, 1.5 \times 10^{15}] \text{ Hz}$ is the considered frequency range. The optical depth is computed along radial

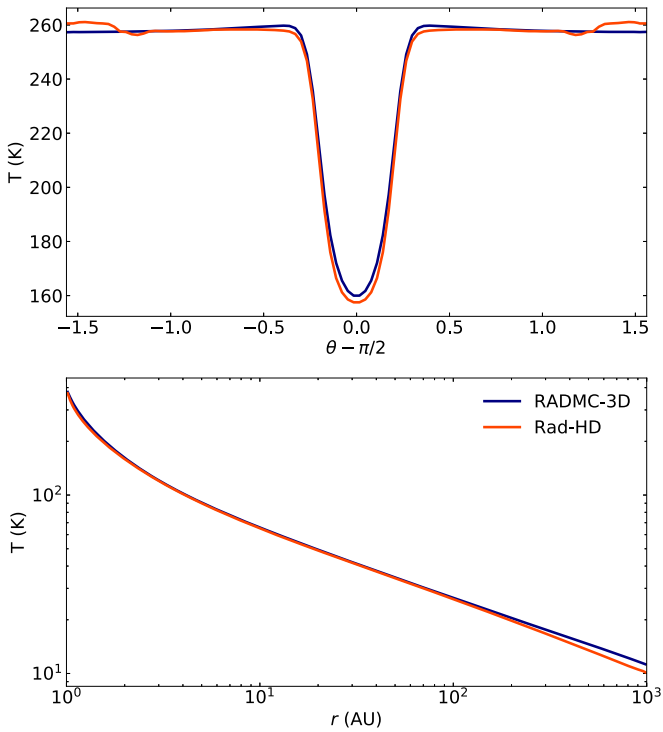


Figure 12. Temperature distributions in the stellar irradiation test obtained with the presented Rad-HD module (orange) and the Monte Carlo radiative transfer code RADMC-3D (blue), shown at $r = 2$ au (top panel) and at the disk midplane (bottom panel).

trajectories as

$$\tau(r, \theta, \nu) = \int_{1 \text{ au}}^r dr' \kappa(\nu) \rho(r', \theta), \quad (45)$$

where $\kappa(\nu)$ is the tabulated frequency-dependent absorption opacity, while scattering is neglected. In the radiation–matter interaction terms (Equation (4)), we compute κ and χ , respectively, as their Planck and Rosseland means evaluated at the local gas temperature.

We integrate the evolution equations of radiation fields and gas energy neglecting the advection terms of the latter, namely,

$$\frac{\partial E}{\partial t} = cG^0 - \nabla \cdot \mathbf{F}_{\text{irr}}. \quad (46)$$

The gas and radiation energy densities are initially set at LTE at a temperature of 10 K in the entire domain. We solve the resulting system of equations on a 2D spherical grid of resolution $N_r \times N_\theta = 240 \times 100$ increasing logarithmically in the radial direction, using the same boundary conditions for the radiation fields as in Section 4.3 and $\hat{c} = c/100$. The same grid is used in the RADMC-3D Monte Carlo computation. In that case, the trajectories of 10^{10} photon packages are tracked and used to compute the disk temperature taking into account the full frequency dependency of the dust opacity. The photons are injected at $r = 0$ with an energy distribution proportional to $B_\nu(T_s)$, and normalized in such a way that the total luminosity equals that of an emitting spherical blackbody with radius R_s and temperature T_s .

In Figure 12, we show 1D slices of the resulting temperature profiles for both simulations, shown as a function of $\theta - \pi/2$ at

$r = 2$ au and as a function of r at the disk midplane. In the first case, both temperature distributions show a good agreement, with relative differences of under 3% of their values. We note that the temperature obtained with Rad-HD exceeds that computed with RADMC-3D close to the azimuthal boundary. This feature is caused by an energy accumulation originated by converging fluxes onto the vertical axis, and disappears if a smaller polar extent is chosen. We obtain in both simulations that the midplane temperature decreases approximately as $r^{-0.4}$ for $r > 10$ au. The difference between the radial temperature profiles stays below 5% between 1 and 2 au, remains under 1% between 2 and 70 au, and steadily grows up to its maximum value of 10% at 1000 au. At that radius, this percentage represents an absolute difference of 1.1 K, and in fact we have verified that this difference stays below 1.2 K for $r > 2.5$ au. Overall, we observe a good agreement between both solutions, comparable for instance with that obtained in Flock et al. (2013) and Mignon-Risse et al. (2020).

5. Conclusions

The goal of this paper was to develop a Rad-HD scheme of general application that is optimized for studies of accreting planets in circumstellar disks. We chose the M1 scheme for this approach as it can handle the anisotropy of the radiation field around an accreting planet and specifically the expected accretion shock.

We presented a radiative transfer module integrated within the HD module of the PLUTO code. The code solves the evolution equations of HD and radiative fields separately through operator splitting, applying substepping for the evolution of radiation fields in order to reduce the overall computational cost. The number of radiation substeps is reduced by applying the RSLA, and two different IMEX-Runge–Kutta schemes can be applied within each substep to integrate the radiation advection and interaction terms. Among other solvers, we have implemented the HLLC Riemann solver for radiation transport introduced in Melon Fuksman & Mignone (2019) in the context of Rad-RMHD. The code has been adapted to all available geometries included in PLUTO, is fully parallel, and can be implemented in rotating frames provided that the relativistic corrections to the radiation fields when transformed into such frame are negligible, which is particularly useful in global simulations of circumstellar disks and planetary accretion.

We tested the code in different scenarios relevant to the physics of protoplanetary disks, paying particular attention to the behavior of the solutions when different values of the speed of light are chosen. In the considered radiative shocks benchmarks, we observe that subcritical shock solutions are accurate in a broader \hat{c} range than supercritical shocks. The obtained solutions with $\hat{c} = c$ are in agreement with those reported in other works. We estimated the energy loss caused by the RSLA when energy is introduced into the system from the domain boundaries, obtaining approximate lower bounds to the value of \hat{c} . On the other hand, all runs of the 1D vertical diffusion test in a static disk yield energy and flux distributions that converge to the exact stationary solution in different timescales. We observe slight deviations with respect to the exact solution caused by operator splitting error, that get reduced for decreasing \hat{c} .

We applied the code in 2D simulations of viscously heated protoplanetary disks. The obtained solutions are almost

indistinguishable for \hat{c} values larger than the theoretical limit obtained by applying the validity conditions for the RSLA given in Skinner & Ostriker (2013), and are clearly different for lower values. We obtain that the mean convective and radiative heat fluxes in the vertical direction are reduced for decreasing \hat{c} . We also compare these effects in terms of the time-averaged Nusselt number, whose maximum value decreases when \hat{c} is reduced.

We ran 3D HD and Rad-HD simulations of the gas accretion by a giant Jupiter mass core embedded in a protoplanetary disk. We computed the joint evolution of gas and radiation for three different opacity regimes, observing in every case the formation of spiral arms and a hot rotating gas envelope surrounding the planetary core. For the highest employed opacity, the LTE limit is recovered and the solutions are almost identical to those obtained with HD. For lower opacities, the produced envelope becomes more compact due to the lower pressure support caused by radiative losses and rotates faster due to conservation of angular momentum. In such cases, a transition between the diffusion and almost free-streaming regimes is observed as radiation is transported away from the envelope and the spirals. After 40 orbits, the simulation with the intermediate opacity value shows a sharper gap at the planet location and overall lower temperatures than in the HD adiabatic case. We computed the total mass inside the planet’s Roche lobe as a function of time, showing higher values in the Rad-HD case, which could indicate a faster planet growth for decreasing opacity.

We further studied the performance of our scheme in standard tests for comparison with other methods. We verified the accuracy of the IMEX-SSP2(2,2,2) method, which shows a convergence order closer to 2 than the operator-split scheme by Skinner & Ostriker (2013). We studied the parallel performance of the code in 2D and 3D setups using up to 1280 processors, in which case we obtain efficiencies of 93% in 2D and 85% in 3D. Future developments of this module will include the implementation of the adaptive mesh refinement routines already present in PLUTO. The module presented in this work will be included in forthcoming releases of PLUTO, which can be downloaded from <http://plutocode.ph.unito.it/>.

Future studies of our M1 Rad-HD scheme will expand on the modeling of gas accretion onto planetary cores, the use of realistic Rosseland and Planck opacities, and higher resolutions achieved through adaptive mesh refinement. Currently we are comparing our results on the temperature structure around the planet and the intensity of radiation with detailed Monte Carlo continuum radiative transfer simulations (Krieger & Wolf (2020)), in a collaboration on deriving the characteristics of exoplanets from observations of for various current and future instruments including ALMA (Kurz et al. 2002), PIONIER (Le Bouquin et al. 2011), and MATISSE (Lopez et al. 2014).

We thank Oliver Voelkel and Rolf Kuiper for sharing their manuscript and insight into M1 methods for disk simulations using the PLUTO code. The research of J.D.M.F. and H.K. is supported by the German Science Foundation (DFG) under the priority program SPP 1992: “Exoplanet Diversity” under contract KL 1469/16-1. M.F. received funding from the European Research Council (ERC) under the European Union’s Horizon 2020 research and innovation program (grant agreement No. 757957). We thank our collaboration partners on this project in Kiel, under contract (WO 857/17-1),

Sebastian Wolf and Anton Krieger for fruitful discussions and guidance for the synchronization of both project parts. This research was also supported by the Munich Institute for Astro- and Particle Physics (MIAPP) of the DFG cluster of excellence “Origin and Structure of the Universe” and was performed in part at KITP Santa Barbara by the National Science Foundation under grant No. NSF PHY11-25915. We also thank the anonymous referee for constructive comments that helped to improve the quality of this work.

Appendix Performance Tests

A.1. Damped Linear Waves

We tested the convergence rate of the implemented IMEX schemes by investigating the evolution of damped linear radiation waves in a static absorbing medium. We reproduced the setup by Skinner & Ostriker (2013), in which the material’s emission is neglected. This leads to the following evolution equations for the radiation quantities:

$$\begin{aligned} \frac{1}{\hat{c}} \frac{\partial E_r}{\partial t} + \nabla \cdot \mathbf{F}_r &= -\kappa_r \rho E_r \\ \frac{1}{\hat{c}} \frac{\partial \mathbf{F}_r}{\partial t} + \nabla \cdot \mathbb{P}_r &= -\kappa_r \rho \mathbf{F}_r^x. \end{aligned} \quad (\text{A1})$$

We define the initial condition as

$$\mathcal{U}_r(\mathbf{r}, 0) = \mathcal{U}_0(\mathbf{r} \cdot \mathbf{n}) = \left[E_0 + \varepsilon \sin\left(\frac{2\pi}{\lambda} \mathbf{r} \cdot \mathbf{n}\right) \right] \begin{pmatrix} 1 \\ \mathbf{n} \end{pmatrix}, \quad (\text{A2})$$

where \mathbf{n} is a unit vector indicating the direction of the radiative flux and the E_0 , ε , and λ parameters correspond, respectively, to the mean value, the amplitude, and the wavelength of the initial state. This initial condition satisfies $\|\mathbf{F}_r\| = E_r$, and therefore the pressure tensor is proportional to E_r as $\mathbb{P}_r = E_r \mathbf{n} \mathbf{n}$ (see Section 2). The exact solution of this initial value problem is a damped wave of the form

$$\bar{\mathcal{U}}_r(\mathbf{r}, t) = \mathcal{U}_0(\mathbf{r} \cdot \mathbf{n} - \hat{c} t) e^{-\rho \kappa_r \hat{c} t}, \quad (\text{A3})$$

which consistently maintains the free-streaming condition $\|\mathbf{F}_r\| = E_r$ throughout its entire evolution. We parameterize the direction of propagation as $\mathbf{n} = (\cos \alpha \cos \beta, \cos \alpha \sin \beta, \sin \alpha)$, with $\alpha \in [0, \pi]$ and $\beta \in [0, 2\pi]$.

We computed the evolution of \mathcal{U}_r using the IMEX1 and IMEX-SSP2(2,2,2) methods (see Section 3.3). Simulations were run in 1D, 2D, and 3D in each case, using the HLL and HLLC Riemann solvers. We chose the parameters $E_0 = 1$, $\varepsilon = 10^{-6}$, $\lambda = 1$, and $\hat{c} = c = 1$. We conducted in each case a resolution study using uniform Cartesian grids with periodic boundary conditions in every direction. The employed resolution is parameterized with an integer N in the range $[2^4, 2^8]$. We use the domains $[0, 1]$, $[0, \sqrt{5}] \times [0, \sqrt{5}/2]$, and $[0, 3] \times [0, 3/2] \times [0, 3/2]$ and the angles $(\alpha, \beta) = (0, 0)$, $(0, \tan^{-1}(2))$, and $(\tan^{-1}(2/\sqrt{5}), \tan^{-1}(2))$ in 1D, 2D, and 3D, respectively. In this way, the domain length in each direction corresponds to one wave period. The time step is set as in Equation (21), with $C_a = 0.3$.

For each integration method and resolution, we compute the L_1 -difference $\delta \mathcal{U}_r$ between the obtained \mathcal{U}_r and the exact

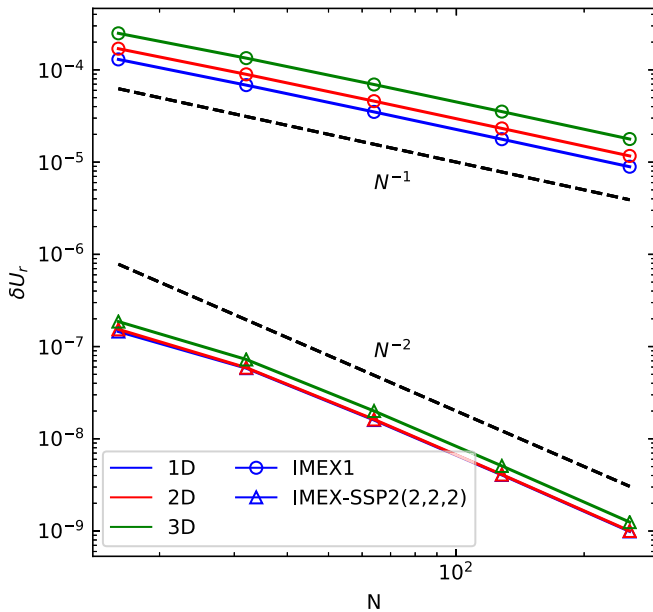


Figure 13. 2-norm of $\delta\mathcal{U}_r$ for the 1D, 2D, and 3D damped wave test (blue, red, and green solid lines, respectively) as a function of the resolution parameter N . The circle and triangle symbols correspond to computations carried out with the IMEX1 and IMEX-SSP2(2,2,2) methods, respectively. Dashed black lines show the ideal convergence slope for each method.

solution at $t = 1$, i.e., after one period, defined as

$$\delta\mathcal{U}_r = \frac{1}{2N^d} \sum_{i,j,k} |\mathcal{U}_{r,i,j,k} - \bar{\mathcal{U}}_{r,i,j,k}|_1, \quad (\text{A4})$$

where $|\cdot|_1$ denotes the L_1 norm, d is the problem’s dimension, and the indices (i, j, k) run over all grid cells. The obtained values of $\delta\mathcal{U}_r$ are shown in Figure 13 as a function of N . In each case, the numerical solutions converge to the exact ones at the expected rate, i.e., 1 for IMEX1 and 2 for IMEX-SSP2(2,2,2). The errors computed with the latter are comparable to those reported by Skinner & Ostriker (2013), while the IMEX-SSP2(2,2,2) method is closer to order 2 accuracy. It is remarkable that the errors computed with IMEX-SSP2(2,2,2) are around 3 orders of magnitude smaller than with IMEX1, since the former method computes the mean value of the wave much more accurately than the latter. Unlike in the Riemann shock tests in Melon Fuksman & Mignone (2019), in this case we observed no difference between the accuracy of the solutions computed with the HLL and HLLC solvers, since no contact waves are created when radiation transport occurs in only one direction.

A.2. Marshak Wave

The Marshak wave test, named after the work by Marshak (Marshak 1958), is a radiative transfer problem generally used as a standard benchmark for Rad-HD codes that studies the propagation of a planar radiation front into a purely absorbing, cold, homogeneous medium. In this setup, radiation is injected from the left boundary of a 1D domain defined as $x \geq 0$. A semi-analytic solution of this problem is given in Su & Olson (1996) under the diffusion and Eddington approximations, i.e., assuming the validity of Equation (15) and assuming constant opacity. Additionally, as proposed by Pomraning (1979), it is assumed as a simplification that the constant-volume heat

capacity c_v of the material is proportional to T^3 , where $c_v = \partial(\rho\epsilon)/\partial T$ (see Equation (2)). Taking $\mathbf{v} = \mathbf{0}$, this is equivalent to redefining the gas temperature in such a way that $E \propto T^4$.

We approached this problem by solving the Rad-HD equations with constant $\rho = 1$ and null velocity, taking $c = \hat{c} = a_R = \kappa = \rho = 1$ and $E = T^4$. In the notation used by Su & Olson (1996), the latter choice corresponds to setting $\epsilon = 1$. Unlike in that work, we do not use the diffusion and Eddington approximations, and instead compute the radiation flux by means of the last of Equation (1).

For a better comparison with other works, we define the computational domain as $x \in [0, 100/\sqrt{3}]$. In this way, the total optical depth of the domain is $100/\sqrt{3} \approx 57.7$. We initially set uniform gas and radiation energy densities as $E_r = E = 10^{-8}$, while $F_r^x = 0$. These same relations are also imposed for $t > 0$ at the right boundary, while on the left one we use the Marshak boundary condition given by

$$E_r + 2F_r^x = 4F_{\text{inc}}, \quad (\text{A5})$$

where $F_{\text{inc}} = 1/4$ is the flux incident on the $x = 0$ surface. This condition is imposed by computing E_r at $x = 0$ using the semi-analytical solution by Su & Olson (1996), and subsequently using Equation (A5) to compute F_r^x . We employ the IMEX1 method with the HLLC solver and the second-order linear TVD Van Leer reconstruction scheme, with $C_a = 0.4$.

The obtained values for E and E_r are shown in Figure 14 at $t = 1, 10$, and 100 at the resolutions of 128 and 1024 zones, together with their semi-analytical values. In each case, the left boundary condition creates a freely streaming radiation front that propagates into the domain while transitioning into the diffusion regime as it interacts with increasingly large amounts of matter. At $t = 1$, the reduced radiative flux reaches $f = 1$ at the wave front, while at $t = 100$ this value is reduced to 0.25, which corresponds to $\xi \approx 0.36$ (see Equations (12)–(14)). In the same way, the radiation and gas energy densities are largely different at $t = 1$ and almost identical at $t = 100$, since they are both equal to T^4 in LTE.

As expected, the numerical solutions approach the semi-analytical ones as the diffusion regime is reached. The agreement between both solutions is comparable to that obtained in González et al. (2007) and Skinner & Ostriker (2013). The obtained solutions are similar to those shown in Skinner & Ostriker (2013) with the same chosen parameters and at the same resolutions. However, as in González et al. (2007), we still observe at later times a difference between the semi-analytic and numerical solutions that is not apparent in Skinner & Ostriker (2013), possibly due to the different operator splitting scheme used in that work. Such a difference is however expectable, since the wave front is outside the diffusion regime through almost its entire evolution.

A.3. Parallel Performance

We tested the parallel scalability of the presented code in strong scaling through 2D and 3D computations. With this purpose, we set up a configuration in which a blast wave is created from an overpressurized region of radius $R_0 = 0.1$ in the center of a cubic domain of side length $L = 1$. All fields are initially uniform both outside and inside of this region, with $\rho = p_g = 100$ inside and $\rho = p_g = 1$ outside. Both ρ and p_g decrease linearly from their maximum to their minimum values

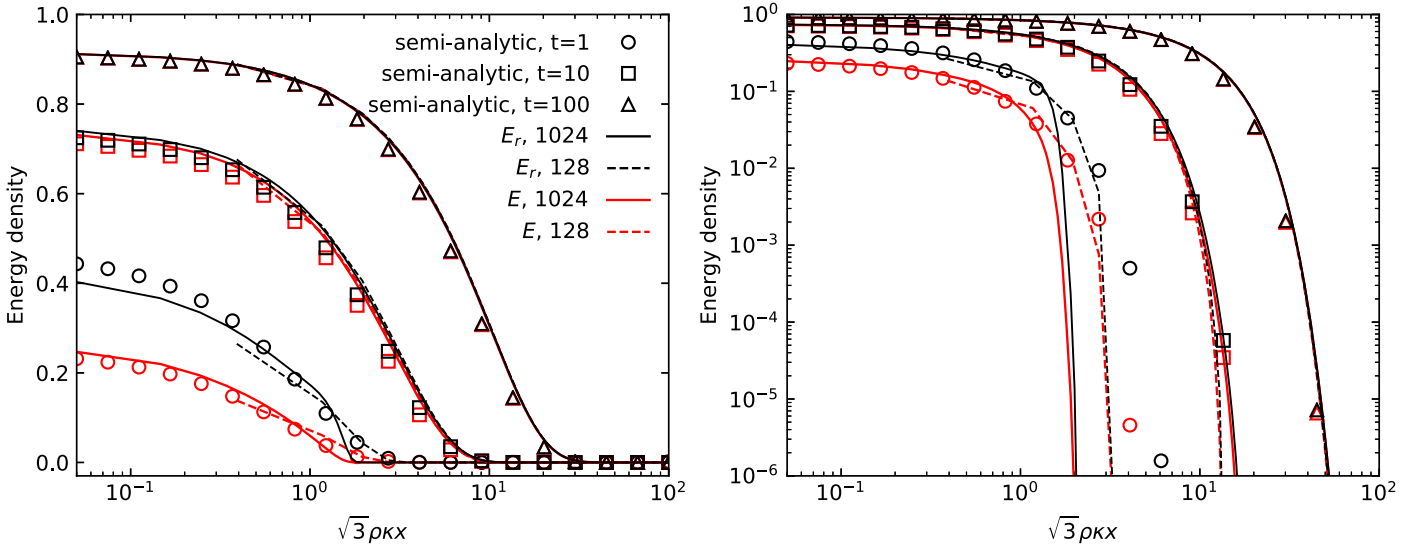


Figure 14. Gas (red) and radiation (black) energy densities obtained in the Marshak wave test at $t = 1, 10,$ and $100,$ represented on semi-log (left panel) and log-log (right panel) scales as a function of $\sqrt{3}\rho\kappa x.$ Solid and dashed lines correspond to numerical values obtained at resolutions of 1024 and 128 zones, respectively. The semi-analytical solutions by Su & Olson (1996) are shown with circle, square, and triangle symbols at $t = 1, 10,$ and $100,$ respectively.

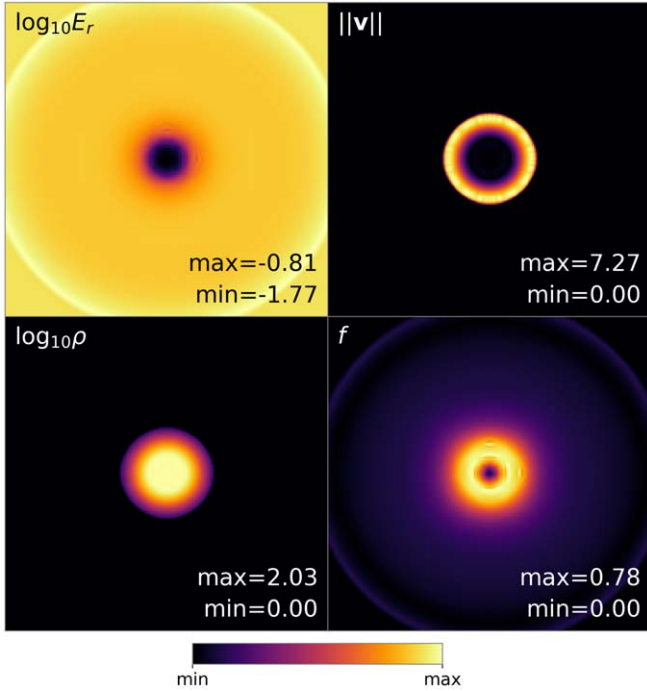


Figure 15. 2D slices at $z = 0$ of the 3D blast-wave test used for the parallel scaling analysis, showing $\log_{10} E_r,$ $\log_{10} \rho,$ $\|v\|,$ and f at $t = 0.007.$

between $r = 0.08$ and $0.1,$ where $r = \sqrt{x^2 + y^2 + z^2}$ ($r = \sqrt{x^2 + y^2}$) in 3D (2D). Initial LTE is imposed in the entire domain, with $a_R = \mu m_p / k_B = 1$ and $\Gamma = 1.4.$ We set as well $\kappa = 0.5,$ $\sigma = 0,$ $c = 10^5,$ and $\hat{c} = 10^2.$

Computations have been performed on uniform Cartesian grids of 2560^2 and 200^3 zones in 2D and 3D, respectively, for a total time $t = 0.007.$ Final $\log_{10} E_r,$ $\log_{10} \rho,$ $\|v\|,$ and f profiles in the 3D test are shown in Figure 15 at $z = 0.$ Two radiation fronts can be identified in the f profile: an outer front, caused by the initial relaxation of the system, and an inner front, corresponding to the radiative diffusion from the overpressurized region. Matter

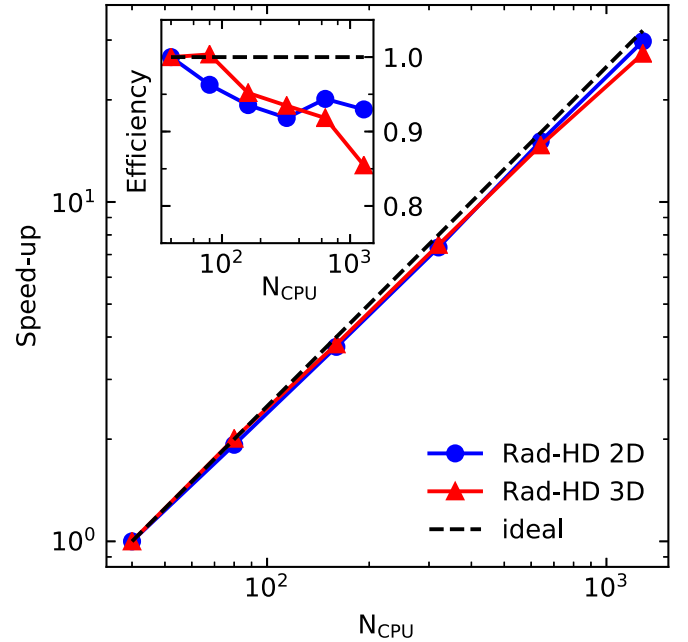


Figure 16. Speed-up factor and scaling efficiency for the 2D (blue) and 3D (red) blast-wave tests as a function of the number of processors. The ideal scaling law (dashed black line) is shown for comparison.

is isotropically accelerated, reaching at that time a maximum velocity of $\|v\| = 7.27$ in the outer boundaries of the central region.

We ran each test using a different number of processors (Intel Skylake 6148 at 2.2 GHz), varying from $N_{\text{CPU}} = 40$ –1280. We increased N_{CPU} in steps of 40 given the 40 cores per node architecture of our system. Corresponding speed-up factors S are shown in Figure 16 as a function of $N_{\text{CPU}},$ computed as $S = T_{\text{ref}} / T_{N_{\text{CPU}}},$ where $T_{N_{\text{CPU}}}$ is the average computation time per step for each $N_{\text{CPU}},$ and $T_{\text{ref}} = T_{40}.$ In the same figure we show the obtained efficiencies for both the 2D and 3D runs, all of which stay above 90% for $N_{\text{CPU}} \leq 512,$ reaching 93% and 85% for $N_{\text{CPU}} = 1280$ in 2D and 3D,

respectively. This scaling behavior is essential to overcome the scale disparity between radiation and HD characteristic speeds, which makes Rad-HD computations approximately 120 times more expensive than HD runs of this test. Some factors that in general affect the scaling efficiency of the code are the chosen domain decomposition, the latency that can arise if the condition $\|F_r\| \leq E_r$ is imposed in only part of the domain, and the increasing number of communications for larger N_{CPU} required, e.g., to define field values at ghost cells and to compute the time step.

ORCID iDs

Julio David Melon Fuksman  <https://orcid.org/0000-0002-1697-6433>

Hubert Klahr  <https://orcid.org/0000-0002-8227-5467>

Mario Flock  <https://orcid.org/0000-0002-9298-3029>

Andrea Mignone  <https://orcid.org/0000-0002-8352-6635>

References

- Alexiades, V., Amiez, G., & Gremaud, P.-A. 1996, *CNME*, 12, 31
- ALMA Partnership, Brogan, C. L., Pérez, L. M., et al. 2015, *ApJL*, 808, L3
- Audit, E., Charrier, P., Chièze, J. P., & Dubroca, B. 2002, arXiv:astro-ph/0206281
- Ayliffe, B. A., & Bate, M. R. 2012, *MNRAS*, 427, 2597
- Beckers, J. M. 1992, *SJNA*, 29, 701
- Bell, K. R., Cassen, P. M., Klahr, H. H., & Henning, T. 1997, *ApJ*, 486, 372
- Bell, K. R., & Lin, D. N. C. 1994, *ApJ*, 427, 987
- Bodenheimer, P., & Pollack, J. B. 1986, *Icar*, 67, 391
- Bucciantini, N., & Del Zanna, L. 2013, *MNRAS*, 428, 71
- Cabot, W. 1996, *ApJ*, 465, 874
- Colombo, S., Ibgui, L., Orlando, S., et al. 2019, *A&A*, 631, A41
- Commerçon, B., Teyssier, R., Audit, E., Hennebelle, P., & Chabrier, G. 2011, *A&A*, 529, A35
- Courant, R., Friedrichs, K., & Lewy, H. 1928, *MatAn*, 100, 32
- D'Angelo, G., & Bodenheimer, P. 2013, *ApJ*, 778, 77
- Davis, S. W., Stone, J. M., & Jiang, Y.-F. 2012, *ApJS*, 199, 9
- Decampli, W. M., Cameron, A. G. W., Bodenheimer, P., & Black, D. C. 1978, *ApJ*, 223, 854
- Draine, B. T., & Lee, H. M. 1984, *ApJ*, 285, 89
- Dullemond, C. P., Juhasz, A., Pohl, A., et al. 2012, RADMC-3D: A Multi-purpose Radiative Transfer Tool, Astrophysics Source Code Library, ascl:1202.015
- Ensmann, L. 1994, *ApJ*, 424, 275
- Flock, M., Fromang, S., González, M., & Commerçon, B. 2013, *A&A*, 560, A43
- Flock, M., Fromang, S., Turner, N. J., & Benisty, M. 2017, *ApJ*, 835, 230
- Flock, M., Ruge, J. P., Dzyurkevich, N., et al. 2015, *A&A*, 574, A68
- Fortier, A., Alibert, Y., Carron, F., Benz, W., & Dittkrist, K. M. 2013, *A&A*, 549, A44
- Fromang, S., Lyra, W., & Masset, F. 2011, *A&A*, 534, A107
- Gammie, C. F. 1996, *ApJ*, 457, 355
- Gnedin, N. Y., & Abel, T. 2001, *NewA*, 6, 437
- González, M., Audit, E., & Huynh, P. 2007, *A&A*, 464, 429
- Gottlieb, S., & Shu, C. W. 1996, NASA CR-201591 ICASE, Tech. Rep. 96
- Hayes, J. C., & Norman, M. L. 2003, *ApJS*, 147, 197
- Jiang, Y.-F., Stone, J. M., & Davis, S. W. 2012, *ApJS*, 199, 14
- Klahr, H. 2007, in IAU Symp. 239, Convection in Astrophysics, ed. F. Kupka, I. Roxburgh, & K. L. Chan, 405
- Klahr, H., & Bodenheimer, P. 2006, *ApJ*, 639, 432
- Klahr, H., & Kley, W. 2006, *A&A*, 445, 747
- Klahr, H. H., Henning, T., & Kley, W. 1999, *ApJ*, 514, 325
- Kley, W., & Nelson, R. P. 2012, *ARA&A*, 50, 211
- Kolb, S. M., Stute, M., Kley, W., & Mignone, A. 2013, *A&A*, 559, A80
- Krieger, A., & Wolf, S. 2020, *A&A*, 635, A148
- Kurz, R., Guilloteau, S., & Shaver, P. 2002, *Msngr*, 107, 7
- Lambrechts, M., & Johansen, A. 2012, *A&A*, 544, A32
- Le Bouquin, J. B., Berger, J. P., Lazareff, B., et al. 2011, *A&A*, 535, A67
- Levermore, C. D. 1984, *JQSRT*, 31, 149
- Levermore, C. D., & Pomraning, G. C. 1981, *ApJ*, 248, 321
- Lin, D. N. C., & Papaloizou, J. 1980, *MNRAS*, 191, 37
- Lopez, B., Lagarde, S., Jaffe, W., et al. 2014, *Msngr*, 157, 5
- Lowrie, R. B., Morel, J. E., & Hittinger, J. A. 1999, *ApJ*, 521, 432
- Lyra, W., Richert, A. J. W., Boley, A., et al. 2016, *ApJ*, 817, 102
- Malygin, M. G., Kuiper, R., Klahr, H., Dullemond, C. P., & Henning, T. 2014, *A&A*, 568, A91
- Manger, N., & Klahr, H. 2018, *MNRAS*, 480, 2125
- Marshak, R. E. 1958, *PhFl*, 1, 24
- McKinney, J. C., Tchekhovskoy, A., Sądowski, A., & Narayan, R. 2014, *MNRAS*, 441, 3177
- Melon Fuksman, J. D., & Mignone, A. 2019, *ApJS*, 242, 20
- Meyer, C. D., Balsara, D. S., & Aslam, T. D. 2012, *MNRAS*, 422, 2102
- Mignone, A., Bodo, G., Massaglia, S., et al. 2007, *ApJS*, 170, 228
- Mignone, A., Flock, M., Stute, M., Kolb, S. M., & Muscianisi, G. 2012a, *A&A*, 545, A152
- Mignone, A., Zanni, C., Tzeferacos, P., et al. 2012b, *ApJS*, 198, 7
- Mignon-Risse, R., González, M., Commerçon, B., & Rosdahl, J. 2020, *A&A*, 635, A42
- Mihalas, D., & Mihalas, B. W. 1984, Foundations of Radiation Hydrodynamics (New York: Oxford Univ. Press)
- Mizuno, H. 1980, *PThPh*, 64, 544
- Mordasini, C., Alibert, Y., Klahr, H., & Henning, T. 2012, *A&A*, 547, A111
- Movshovitz, N., Bodenheimer, P., Podolak, M., & Lissauer, J. J. 2010, *Icar*, 209, 616
- Ormel, C. W., & Klahr, H. H. 2010, *A&A*, 520, A43
- Palenzuela, C., Lehner, L., Reula, O., & Rezzolla, L. 2009, *MNRAS*, 394, 1727
- Pareschi, L., & Russo, G. 2005, *JSCom*, 25, 129
- Pascucci, I., Wolf, S., Steinacker, J., et al. 2004, *A&A*, 417, 793
- Pfeil, T., & Klahr, H. 2019, *ApJ*, 871, 150
- Pollack, J. B., Hubickyj, O., Bodenheimer, P., et al. 1996, *Icar*, 124, 62
- Pomraning, G. C. 1979, *JQSRT*, 21, 249
- Rosdahl, J., & Teyssier, R. 2015, *MNRAS*, 449, 4380
- Rüdiger, G., Arlt, R., & Shalybkov, D. 2002, *A&A*, 391, 781
- Sądowski, A., Narayan, R., Tchekhovskoy, A., & Zhu, Y. 2013, *MNRAS*, 429, 3533
- Schulik, M., Johansen, A., Bitsch, B., & Lega, E. 2019, *A&A*, 632, A118
- Schulik, M., Johansen, A., Bitsch, B., Lega, E., & Lambrechts, M. 2020, *A&A*, 642, A187
- Shakura, N. I., & Sunyaev, R. A. 1973, in IAU Symp. 55, X- and Gamma-Ray Astronomy, ed. H. Bradt & R. Giacconi (Dordrecht: Reidel), 155
- Skinner, M. A., & Ostriker, E. C. 2013, *ApJS*, 206, 21
- Strang, G. 1968, *SJNA*, 5, 506
- Su, B., & Olson, G. L. 1996, *JQSRT*, 56, 337
- Szulágyi, J., Dullemond, C. P., Pohl, A., & Quanz, S. P. 2019, *MNRAS*, 487, 1248
- Szulágyi, J., Masset, F., Lega, E., et al. 2016, *MNRAS*, 460, 2853
- Szulágyi, J., Morbidelli, A., Crida, A., & Masset, F. 2014, *ApJ*, 782, 65
- Szulágyi, J., & Mordasini, C. 2017, *MNRAS*, 465, L64
- Szulágyi, J., Plas, G. v. d., Meyer, M. R., et al. 2018, *MNRAS*, 473, 3573
- Takahashi, H. R., & Ohsuga, K. 2013, *ApJ*, 772, 127
- Toro, E. F. 2009, Riemann Solvers and Numerical Methods for Fluid Dynamics (Berlin: Springer)
- Vaidya, B., Prasad, D., Mignone, A., Sharma, P., & Rickler, L. 2017, *MNRAS*, 472, 3147
- Voelkel, O. 2017, Master's thesis, Univ. Tübingen
- Weih, L. R., Olivares, H., & Rezzolla, L. 2020, *MNRAS*, 495, 2285
- Yamaleev, N. K., & Carpenter, M. H. 2009, *JCoPh*, 228, 4248
- Zel'dovich, Y. B., & Raizer, Y. P. 1967, Physics of Shock Waves and High-temperature Hydrodynamic Phenomena, Vol. 2 (New York: Academic)
- Zhu, Z., Jiang, Y.-F., & Stone, J. M. 2020, *MNRAS*, 495, 3494